Palaeogeography, Palaeoclimatology, Palaeoecology 677 (2025) 113207

Contents lists available at ScienceDirect

Palaeogeography, Palaeoclimatology, Palaeoecology

journal homepage: www.elsevier.com/locate/palaeo

Sedimentary records reveal an early Cambrian active margin setting in the NW Yangtze Block, South China

Zhidong Gu [a,*], Xing Jian [b,*], Xiufen Zhai [a], Xiaotian Shen [b], Shuhuai Ye [b]

[a] Research Institute of Petroleum Exploration and Development (RIPED), PetroChina, Beijing 100083, China
[b] State Key Laboratory of Marine Environmental Science, College of Ocean and Earth Sciences, Xiamen University, Xiamen 361102, China

ARTICLE INFO

Editor: Prof. S Shen

Keywords:
Yangtze Block
Central Longmenshan region
Cambrian
Active margin setting
Sedimentary provenance
Detrital zircon geochronology

ABSTRACT

The Ediacaran to Cambrian sedimentary succession in the Yangtze Block (South China) has long been interpreted as forming in a passive margin setting. However, some recent studies on Cambrian geological records challenge this view. Here, we investigated a relatively complete Cambrian section in the central Longmenshan fold-thrust belt, NW Yangtze Block. Composed primarily of fine-grained siliciclastic rocks with subordinate carbonate rocks, this section was analyzed to constrain its depositional age, sedimentary environments, provenance and tectonic setting, and to address the ongoing controversies. The Cambrian succession exhibits coarsening-upward trends and indicates deep-water basin, slope and fan delta settings with hydrothermal inputs. The depositional ages were constrained as the Cambrian Terreneuvian to Epoch 2 interval (ca. 524–509 Ma), based on correlation of carbonate stable carbon isotope ($\delta^{13}C$) results with the global Cambrian $\delta^{13}C$ reference curve and maximum depositional age constraints from detrital zircon U-Pb geochronology. Sandstones from the Qiongzhusi Formation have abundant volcanic lithic fragments and detrital zircons therein are dominated by Ediacaran–Cambrian ages. Nevertheless, sandstones from the Canglangpu Formation consist of various lithic fragments (including chert, metamorphic, volcanic and sedimentary clasts) and present diverse detrital zircon U-Pb ages (predominant 1000–500 Ma with minor 2600–2100 Ma). Both petrographic and geochemical results reveal that the Cambrian sediments are compositionally immature and were derived from proximal sources. Detrital zircon (635–500 Ma) trace elemental compositions denote a continental arc origin. Collectively, these results support proximal arc-related orogenic sources for the early Cambrian clastic sediments, contradicting previous proposals of distal orogenic sources. We propose that the Cambrian depositional succession was formed in an active margin setting in response to the Proto-Tethys Ocean subduction beneath the NW Yangtze Block. Our findings represent a significant advance towards understanding the Ediacaran–Cambrian transition and the role of the South China Craton in the Gondwana assembly process.

1. Introduction

The Ediacaran to Cambrian transition witnessed a remarkable interval in the Earth's history for biological evolution (Grotzinger et al., 1995; Amthor et al., 2003; Marshall, 2006; Wood et al., 2019; Wu et al., 2022; Myrow et al., 2024), oceanic geochemical variation (Rothman et al., 2003; Shields, 2007; Guo et al., 2013; Wen et al., 2015; Li et al., 2017; Ackerman et al., 2022), marine redox fluctuation (Kimura and Watanabe, 2001; Gao et al., 2016; Zhang et al., 2016; Chang et al., 2018; Wang et al., 2018; Wei et al., 2018; He et al., 2019; Wu et al., 2021a, 2022), and global continental configuration (McKenzie et al., 2014; Domeier, 2018; Yang et al., 2020; Merdith et al., 2017, 2021). During this period, most continents and microterranes amalgamated in response to the assembly of Gondwana (Cawood et al., 2013; Cawood et al., 2018; Domeier, 2018; Li et al., 2018a; Yang et al., 2020). The South China Craton (Fig. 1A), which comprises the present-day Yangtze Block in the west and the Cathysian Block in the east, is generally considered as a component of Gondwana and had been positioned along the northwestern margin of East Gondwana (Duan et al., 2011; Cocks and Torsvik, 2013; Xu et al., 2013, 2014; Chen et al., 2016; Li et al., 2018b; Yang et al., 2020; Merdith et al., 2017, 2021). From the perspective of global paleogeographic reconstruction, the present-day Yangtze Block was flanked by the Proto-Tethys Ocean during the Ediacaran and Cambrian, and underwent a tectonic transition from a passive margin setting of the

* Corresponding authors.
E-mail addresses: guzhidong@petrochina.com.cn (Z. Gu), xjian@xmu.edu.cn (X. Jian).

https://doi.org/10.1016/j.palaeo.2025.113207
Received 1 April 2025; Received in revised form 12 August 2025; Accepted 13 August 2025
Available online 13 August 2025

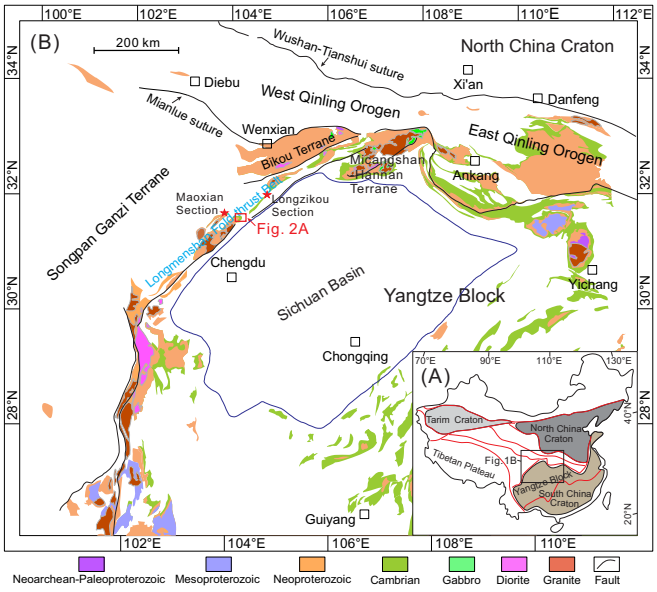

Fig. 1. (A) The tectonic framework of the major cratons in China. (B) A simplified geological map of the NW Yangtze Block, South China, showing the distribution of the Precambrian and Cambrian outcrops.

Ediacaran to an active margin setting of the Cambrian (Cocks and Torsvik, 2013; Cawood et al., 2018; Merdith et al., 2017, 2021). However, whether and how this key tectonic transition is recorded in the Yangtze Block remains poorly constrained.

Most previous studies advocate that the Ediacaran to Cambrian succession in the NW Yangtze Block had formed in a passive margin setting (Jiang et al., 2012; Chen et al., 2016, 2018; Domeier, 2018). Nevertheless, sedimentary records from the NW Yangtze Block (Fig. 1B) document a significant shift from Ediacaran carbonate-dominated to lower Cambrian detritus-dominated successions (Gu et al., 2016, 2023b; Chen et al., 2018). Particularly, the lower Cambrian in most areas is characterized by thick, reverse grading clastic successions, from shales to conglomerates intercalated with minor carbonates (Gu et al., 2021). However, provenance and tectonic setting of the thick lower Cambrian sedimentary records have received limited attention. Some investigators attributed these clastic sediments to exotic source terranes (such as the Himalaya, North India and Qiangtang terranes), linked to Gondwana assembly-related orogenesis (Duan et al., 2011; Chen et al., 2016, 2018; Yang et al., 2020; Han et al., 2024). Most of these provenance interpretations relied predominantly on detrital zircon records, specifically, the observed similarity in zircon age populations between the Cambrian NW Yangtze Block and the distant exotic terranes. Although detrital zircon geochronology (and Hf isotopes) represents a powerful tool in tracing sediment provenance, biases in detrital zircon studies are also prevailing, probably resulting in misleading provenance interpretations (e.g., Malusà et al., 2013; Shen et al., 2024; Jian et al., 2024 and references therein). By contrast, based on an integrated study combining geological, geochemical and geophysical evidence from the north Longmenshan region, Gu et al. (2023b) put forward a new hypothesis that the lower Cambrian clastic rocks had proximal sources and were deposited in an active margin setting due to the subduction of the Proto-Tethys Ocean under the NW Yangtze Block and the associated Motianling orogeny. As a result, an early Cambrian foreland basin was formed in the Longmenshan region owing to the orogenic loading northwestward and lithospheric flexure. Recently, Deng et al. (2025) investigated early Cambrian volcanic rocks from the Maoxian section in the central Longmenshan region (Fig. 1B) and these rocks were explained as products of the Proto-Tethys Ocean subduction.

In this contribution, we investigated the Cambrian Dawuji section (Fig. 2A) in the central Longmenshan region, NW Yangtze Block. This

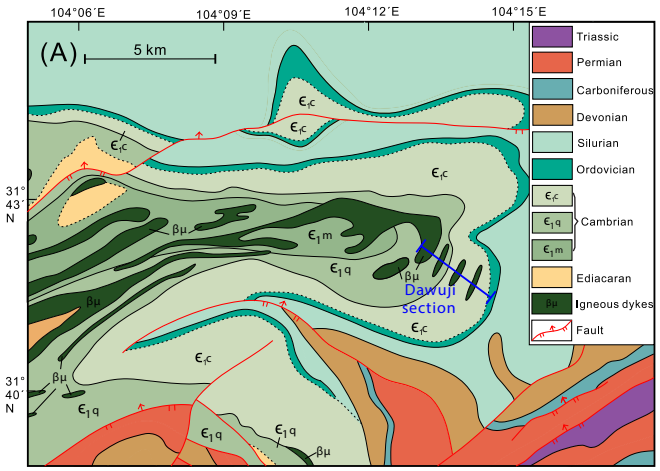

Stratigraphic unit		Thick-ness (m)	Lithology	Description
Ordovician	Baota Fm.	0-90		dominated by limestone
Cambrian	Canglangpu Fm.	300-700		carbonate-rich sandstone, lithic sandstone, siltstone
	Qiongzhusi Fm.	600-1000		mudstone, marlstone, siltstone, back shale, intruded by mafic rocks
	Maidiping Fm.	160-550		chert, dolomite, limestone, carbonaceous shale, intruded by mafic rocks
Ediacaran	Dengying Fm.	700-1000		dominated by dolomite, with subordinate shale, chert and silstone
(B)	Doushantuo Fm.	0-100		dolomite, sandy mudstone, siltstone, sandstone

Fig. 2. Geological map of the study area showing stratigraphic successions and samples sites, modified from the regional geological map of China (1:200000). Note that the Cambrian strata were widely intruded by mafic dykes (involving gabbro and diabase).

section comprises relatively complete lower Cambrian sedimentary successions, characterized by thick reverse grading clastic rocks with minor carbonate rocks. Study on this section can provide useful clues for deciphering provenance (distant or proximal sources) and tectonic setting (passive or active margins) of the lower Cambrian sedimentary rocks. We performed comprehensive field-based sedimentological, petrographic, mineralogical, geochemical and zircon U-Pb-Hf isotopic analyses to interpret depositional process, sediment provenance and tectonic setting of the lower Cambrian sedimentary records.

2. Geological setting

2.1. The Longmenshan fold-thrust belt and surrounding tectonic domains

The Yangtze Block is the northwest part of the South China Craton (Fig. 1A). Major tectonic domains within and around the northwestern Yangtze Block include the Sichuan Basin, the Micangshan-Hannan terrane, the Longmenshan fold-thrust belt, the Bikou terrane, the West Qinling orogen and the Songpan-Ganzi terrane (Fig. 1B). The NE-trending Longmenshan fold-thrust belt defines the northeastern margin of the Tibetan Plateau, which marks a sharp topographic transition from plateau to plain with an elevation drop of ca. 4000 m over ca. 50 to 100 km (Burchfiel et al., 1995; Chen and Wilson, 1996; Xue et al., 2017; Xie et al., 2020). The Longmenshan fold-thrust belt extends ca. 500 km long from NE to SW and 50 km width from SE to NW. It is bounded with the Sichuan Basin to the SE, and bounded with the Bikou terrane to the NW, and bounded with the Songpan-Ganzi terrane to the west (Chen and Wilson, 1996; Jia et al., 2006; Li et al., 2012; Xue et al., 2017; Yan et al., 2018) (Fig. 1B).

Within the Longmenshan fold-thrust belt, Neoproterozoic complexes occur as the Precambrian basement, i.e., the Jiaoziding complex in the north (Li et al., 2018a), the Pengguan complex in the middle (Li et al., 2024b), and the Baoxing complex in the south (Dong et al., 2024). Neoproterozoic arc-related magmatic rocks (including plutonic and volcanic rocks, 860–750 Ma) are also widely distributed in the Longmenshan fold-thrust belt (Li et al., 2024a and references therein). These igneous rocks are considered as parts of the Panxi-Hannan arc belt, indicating a long-lived early-mid Neoproterozoic (970–750 Ma) subduction zone along the northern and western Yangtze Block on the northwestern margin of Rodinia (Zhou et al., 2006; Cawood et al., 2018). A thick lower Cambrian volcaniclastic succession (> 1000 m) is present in the central Longmenshan fold-thrust belt (within the Pengguan complex) indicating a period of volcanic activity in the NW Yangtze Block (Deng et al., 2025). There were three major stages of tectonic movements from the Cambrian to Triassic, which are represented by large sedimentary hiatuses and unconformities between the Cambrian and Ordovician, the Silurian and Permian, and the Middle and Late Triassic (Gu et al., 2016; Yan et al., 2018).

The Sichuan basin is an important petroliferous basin in the NW Yangtze Block with very thick sedimentary infill (> 10 km) including Neoproterozoic to Quaternary deposits (Liu et al., 2021). Its early fill, from Ediacaran to Middle Triassic times, is dominated by shallow marine carbonate deposition (Gu et al., 2021). After that, it developed as a foreland basin, infilled by terrestrial sediments. The Micangshan-Hannan terrane is located between the Sichuan Basin and the Qinling orogen. The Precambrian basement includes Paleoproterozoic amphibolite-facies Houhe complex, Meso-Neoproterozoic greenschist-facies Huodiya Group (metasedimentary rocks in the lower part and volcanic rocks in the upper part), Neoproterozoic greenschist-facies Xixiang Group (dominated by metavolcanic rocks) (Hui et al., 2025). Neoproterozoic mafic-ultramafic and granitoid plutons are widely exposed in the Micangshan-Hannan terrane (Dong et al., 2011). The basement rocks and plutons are mainly unconformably overlain by Ediacaran–Silurian carbonates and siliciclastic rocks (Gu et al., 2023c). Neoproterozoic records are widely exposed in the Bikou terrane (Hui et al., 2021; Gu et al., 2023a), including Bikou Group (dominated by volcanic successions) and Hengdan Group (thick, coarsening-upward, deep marine, pelagic- to turbidite-dominated volcaniclastic deposits) in the southeast and northwest parts, respectively. These strata underwent strong deformation and low greenschist facies metamorphism and unconformably overlie the Neoarchean Yudongzhi Group. Several Neoproterozoic gabbroic-granitoid plutons are distributed within the southeastern part of terrane (Hui et al., 2021, 2022). The Songpan-Ganzi terrane is mainly composed of Triassic highly-deformed, slightly-metamorphosed deep-water marine calciclastic and siliciclastic rocks and Late Triassic–Early Jurassic intermediate-acid igneous intrusions (Jian et al., 2019). The Qinling orogen is the product of the Late Triassic collision between the North and South China Cratons along the Mianlue suture (Fig. 1B). The West Qinling orogen, as the west extension of the Qinling orogen, is sandwiched between the Carboniferous-Permian ophiolitic melange to the north and Early-Middle Triassic ophiolitic melange to the south, connecting with the Triassic Andean-type magmatic arc belts of Kunlun orogenic belt in the west (Yan et al., 2014). Similar to the Songpan-Ganzi terrane, Triassic deposits are widely distributed in the West Qinling orogen, whereas Precambrian (limited exposure, named as Baiyigou Group in the southwestern region, Gu et al., 2025) and lower Paleozoic rocks are uncommon in the orogen (Gu et al., 2023b).

2.2. Cambrian stratigraphy in the Longmenshan fold-thrust belt

In most regions of the Longmenshan fold-thrust belt, the Cambrian succession comprises the Maidiping, Qiongzhusi, and Canglangpu Formations from base to top (Fig. 2B; Gu et al., 2021, 2023b). These strata are thought to have accumulated during the Cambrian Terreneuvian to Epoch 2 (Gu et al., 2023b). The Maidiping Formation is mainly composed of interbedded thin chert and shale with phosphoric carbonate, revealing an anoxic setting. The Qiongzhusi Formation is defined by the first occurrence of trilobites, and consists of organic-rich, black shale and is gradually coarsening upward into muddy siltstones and siltstones. The Canglangpu Formation consists of coarsening-upwards medium to thick siltstones, sandstones and conglomerates. There is a set of carbonates or calcareous sandstones (ca. 5–30 m thick) occurred at the base of the formation as a horizon marker. The Canglangpu Formation is generally unconformably overlain by the Ordovician in the central and north Longmenshan regions.

3. Sedimentological descriptions and samples

We carried out three rounds of field work at the Dawuji section (Fig. 2A) to examine the Cambrian sedimentary records in 2019, 2021 and 2023. Sedimentary successions were measured, described and analyzed, and more than 160 samples (mainly including mudstones, siltstones, carbonate-rich mudstones, carbonate rocks and subordinate sandstones and mafic intrusive rocks) were collected for subsequent lab analyses.

3.1. Outcrop descriptions and sedimentological features

The investigated Dawuji section starts with sporadically-exposed gabbro bodies (Bed 0, Fig. 3; Fig. 4A). The Cambrian consists mainly of the Qiongzhusi Formation (Fig. 3, Beds 1–5) and the overlying Canglangpu Formation (Fig. 3, Beds 6–8), which is unconformably overlain by the Ordovician limestones (Fig. 3, Bed 9). The Qiongzhusi Formation is dominated by thin bedded mudstones and siltstones intruded by some gabbros, and the Canglangpu Formation is characterized by the lower slump carbonates and the upper low maturity clastic rocks.

The basal Qiongzhusi Formation (Bed 1) is mainly composed of thin- or intermediate-bedded mixed carbonate-siliciclastic rocks with dominant calcareous siltstone, calcareous fine-grained sandstone, sandy limestone, silty mudstone and calcareous mudstone (Fig. 4B–C). A sandstone lens occurs in the upper part of Bed 1 (Fig. 4E). The thin-bedded fine-grained sedimentary strata are rich in pyrite nodules with a few centimeters in size (Fig. 4D). The Bed 2 consists of thin-bedded muddy siltstones which are rich in banded pyrite (Fig. 4F–G) and was intruded by gabbro along the bedding directions (Fig. 4H). The Beds 3–5 are discontinuously exposed and are mainly composed of black gray, thin-bedded, gabbro-intruded mudstone and silty mudstone (Fig. 5B–C). The limestone slumps (~1–2 m thick) are occasionally present (Fig. 5D). A bed of porous volcaniclastic rock (~5–10 m thick) is intercalated in the black mudstones (Fig. 5E–F). Some layers of pyrite aggregates occur in the black mudstones (Fig. 5G). The top mudstone of Bed 4 was intruded by gabbro (Fig. 5H).

The lower Canglangpu Formation consists mainly of slump limestones intercalated with thin bedded mudstones and siltstones with a thickness of ca. 140 m (Fig. 3; Fig. 6A–D). Diabase intruded into the mudstones at the top of Bed 6. The Bed 7 includes some coarse-grained greywackes (Fig. 6E–F). The Bed 8 is characterized by grayish siltstone and lithic sandstone with coarsening-upward sequences (Fig. 3; Fig. 6G). The Ordovician limestones which are rich in cameroceras fossils unconformably overlie on the Canglangpu Formation sandstones, revealing a major stratigraphic gap between the Cambrian and the Ordovician (Fig. 6H).

3.2. Samples for lab analyses

More than 110 samples were selected for thin section petrographic analysis, and 14 sandstone samples were selected for framework petrography analysis. Three sandstone samples were targeted for transparent heavy mineral analysis. To constrain and correlate the stratigraphic ages, sixty-seven samples were selected for sedimentary

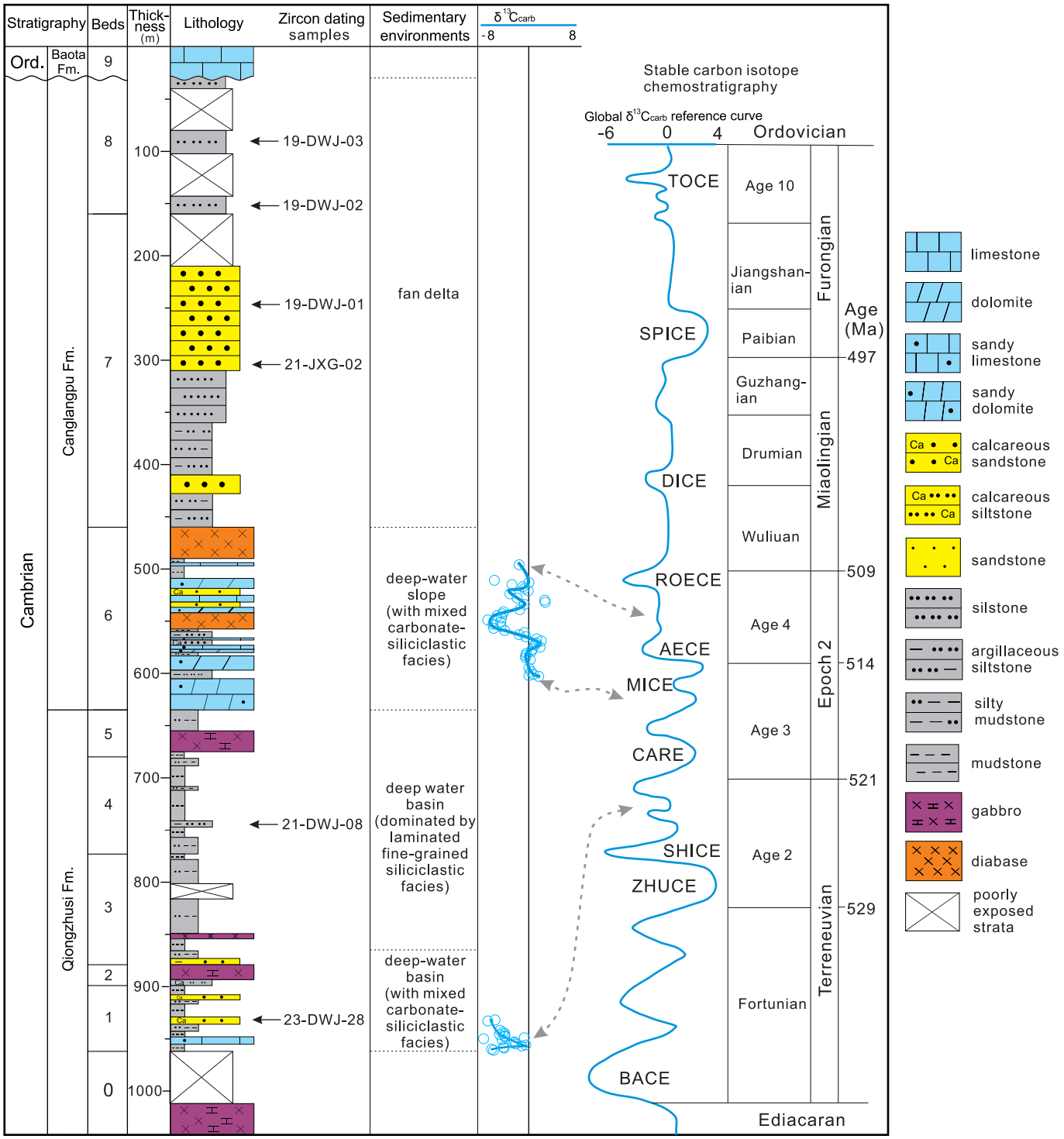

Fig. 3. Lithostratigraphic column showing the Cambrian sedimentary successions at the Dawuji section, detrital zircon dating sample sites, stable carbon isotopic data from sedimentary carbonate samples and the sedimentary environment interpretations. The Global carbon isotope reference curve is modified from Zhu et al. (2019). For detailed descriptions of the carbon isotopic excursions, refer to Zhu et al. (2006, 2019).

carbonate stable carbon isotopic analysis. Moreover, thirty-nine fine-grained siliciclastic rock samples were selected for whole-rock major and trace elemental analyses. Five sandstone and one sand-rich mudstone samples were selected for detrital zircon U-Pb isotopic analysis, and in-situ trace elemental compositions were obtained simultaneously from the dated detrital zircon grains. Some detrital zircon grains from three samples (23-DWJ-28, 21-DWJ-08 and 19-DWJ-01) were subsequently selected for Lu-Hf isotopic analysis. Furthermore, nine and eight representative samples from fine-grained siliciclastic rocks were selected for whole-rock mineralogical and clay mineralogical composition measurements, respectively. All the raw analysis data are presented in the supplemental materials (including Tables S1–S7).

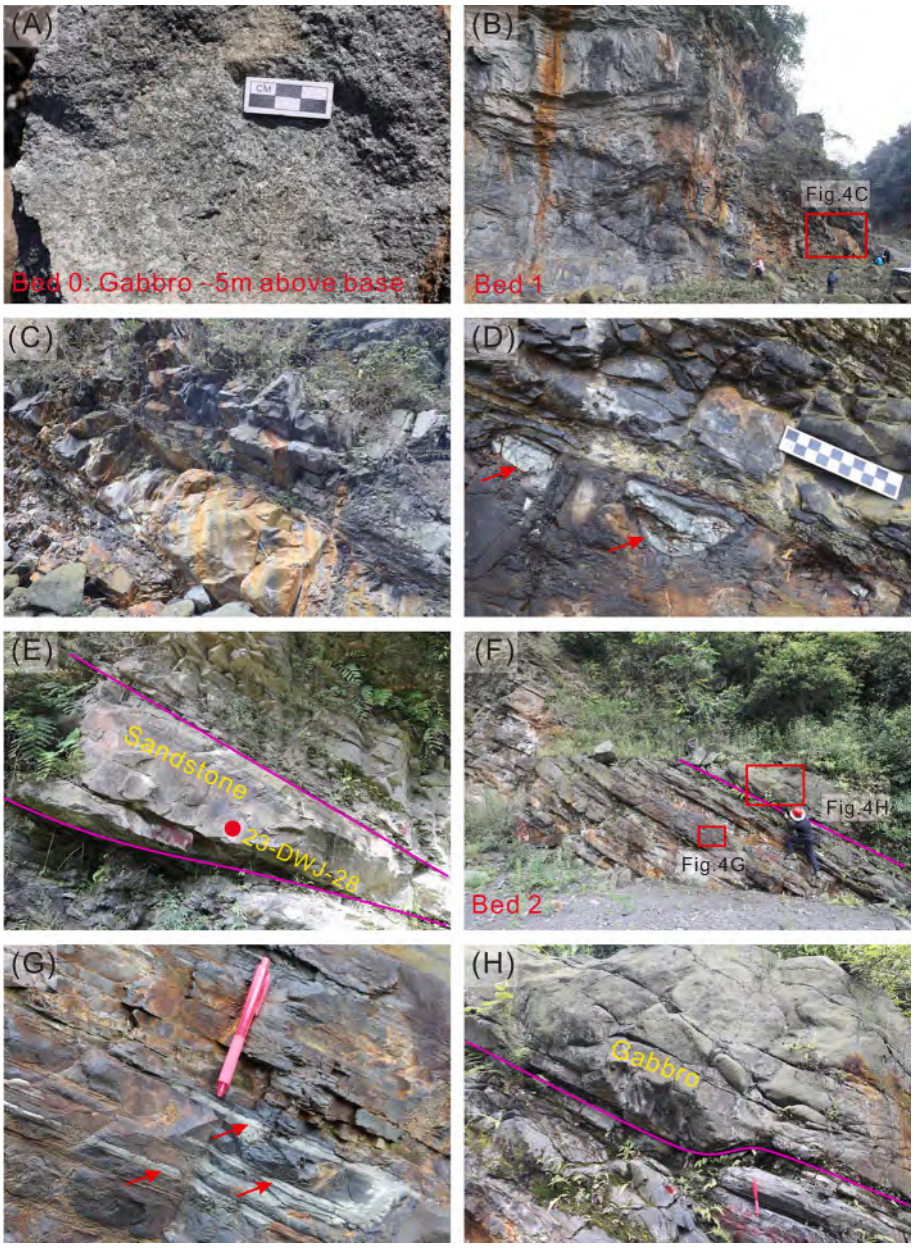

Fig. 4. Representative photographs from the lower parts (Beds 0–2, Fig. 3) of the Cambrian outcrop. (A) Gabbro at the bottom of the profile; (B-D) pyrite nodules (red arrows)-bearing mixed carbonate-siliciclastic strata; (E) thick sandstone layers at the top of Bed 1; (F-H) thin-bedded fine-grained sedimentary rocks intruded by gabbro along the bedding directions. (For interpretation of the references to colour in this figure legend, the reader is referred to the web version of this article.)

4. Methods

4.1. Petrography and sandstone heavy mineral analysis

The collected samples were prepared into 30 μm-thick thin sections for micro-petrographic analysis. Thin sections were observed under a polarizing microscope and the compositional and textural features were described minutely. For carbonate-rich sedimentary rocks, half of each thin section was stained using alizarin red solution before microscopic examination. Model analysis of 14 sandstone samples was performed using the Gazzi-Dickinson method, with greater than 400 points counted per sample (Dickinson, 1985). Selected sandstone samples were analyzed for transparent heavy minerals. The samples were preliminarily crushed and the 63–250 μm fractions were sieved. The sieved fractions were soaked in acetic acid for removing carbonate components and Fe-Mn oxide coatings. Heavy minerals were then separated by heavy liquid tribromomethane (2.89 g/cm^3) from the treated fractions and subsequently weighted and mounted on glass slides with Canada balsam. Transparent heavy minerals were counted and described for compositions and textural features. All the petrographic and transparent heavy mineral analyses were carried out at the Sedimentary Geology Lab, Xiamen University, following the procedures given by Gu et al. (2023a) and Jian et al. (2023).

4.2. Whole-rock mineralogy and clay mineralogy

Mineralogical compositions of selected sedimentary rocks were analyzed using an X'Pert Pro X-ray diffractometer at the Analytical Laboratory, Beijing Research Institute of Uranium Geology. For whole-rock mineralogical analysis, the samples were first powdered to 200 mesh and the rock powders were then scanned using the X-ray diffractometer. For clay mineralogical analysis, loose samples were soaked in

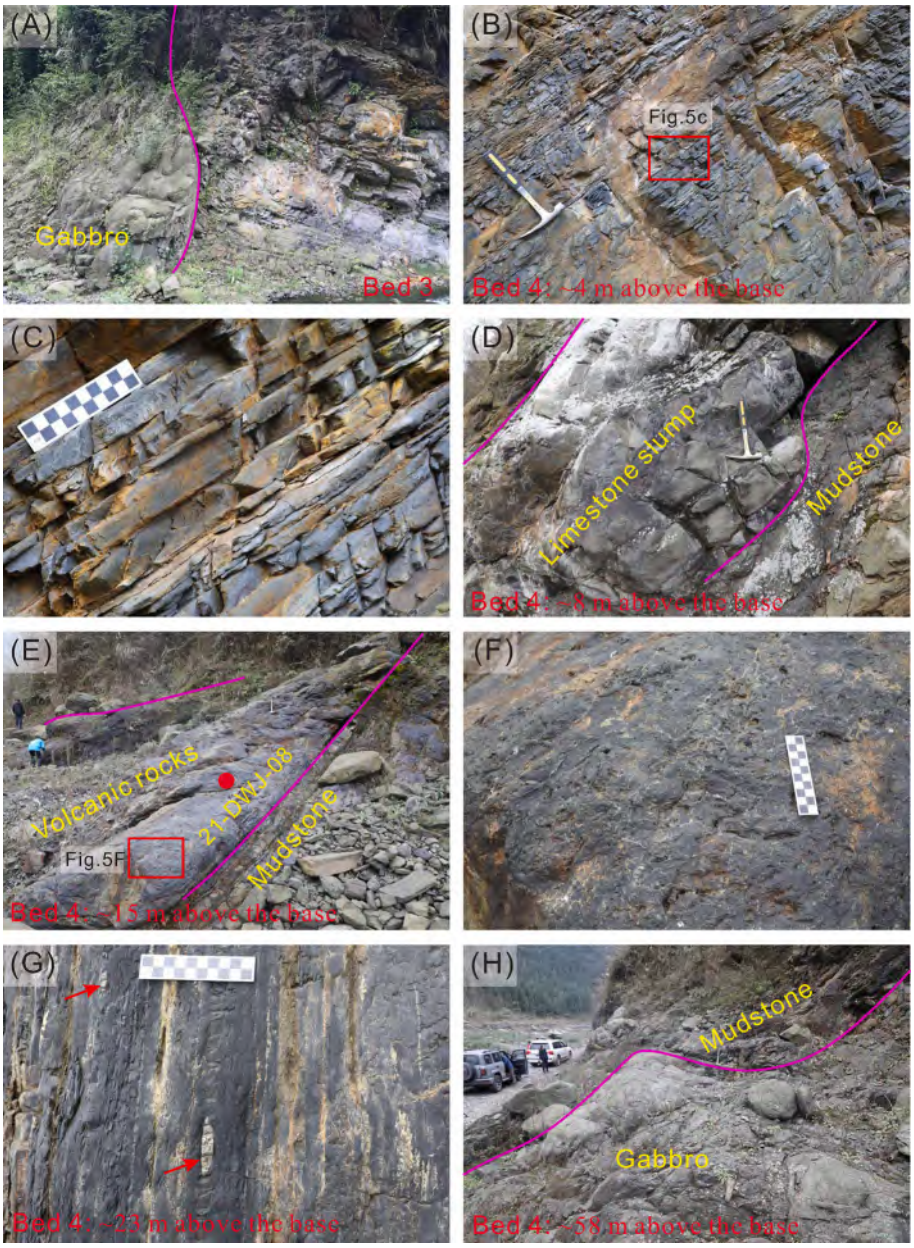

Fig. 5. Representative photographs from the middle parts (Beds 3–4, Fig. 3) of the Cambrian outcrop. (A) fine-grained sedimentary rocks intruded by gabbro; (B-C) representative thin-bedded rocks from Bed 4; (D) limestone slump from the mixed carbonate-siliciclastic strata from Bed 4; (*E*-F) volcanic rocks from Bed 4; (G) pyrite-rich thin-bedded mudstones; (H) mudstone strata intruded by gabbro.

deionized water and the particles <2 μm were separated according to the Stoke's law. The separated clay particles were made to oriented mounts. Air-dried, ethylene glycol-saturated and heated mounts were successively scanned using the X-ray diffractometer. All the XRD scanning data were treated using an MDI jade software for smoothing, peak value extraction and mineral phase identification. The semi-quantitative compositions were then determined.

4.3. Whole-rock major and trace element geochemical analyses

The whole-rock major and trace element analyses were conducted at the Analytical Laboratory, Beijing Research Institute of Uranium Geology. All the samples were crushed and powered to less than 200 meshes for elemental analysis. The Loss on ignition (LOI) values were obtained by measuring the weight loss after heating the sample powders at 980 °C. Before major element determination, the sample powders and the lithium metaborate flux were mixed in 1:10, then fused at 1050 °C in a Pt-Au crucible and were made to glass disks after cooling. Major element compositions of the well-mixed glass disks were determined using an Axios-mAX X-ray fluorescence (XRF) spectrometer. Trace element compositions were determined using an ELEMENT XR Inductively Coupled Plasma Mass Spectrometry (ICP-MS). Before the mass spectrum analysis, the sample powders were accurately weighed (25 mg) and completely dissolved by Hf-HNO_3-$HClO_4$ mixture acid solutions in high-pressure-resistant Teflon beakers. The solutions were finally diluted with 1 % HNO_3 to 50 ml for trace element determination.

4.4. Carbonate stable carbon isotopic analysis

Sedimentary carbonate stable carbon isotopic analysis was conducted at the Analytical Laboratory, Beijing Research Institute of Uranium Geology. The regular phosphoric acid method was used to produce

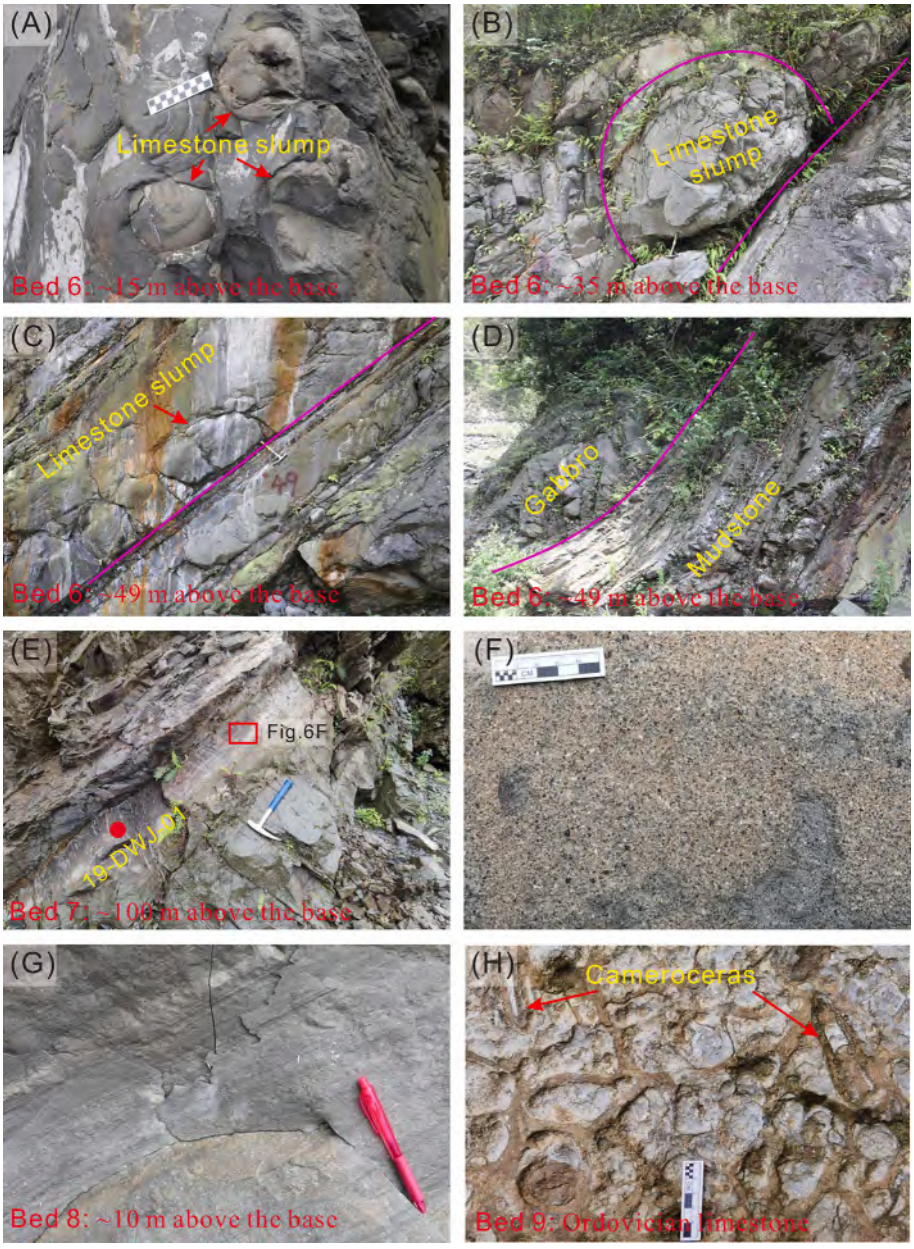

Fig. 6. Representative photographs from the upper parts (Beds 6–9, Fig. 3) of the Cambrian outcrop. (A-C) representative limestone slump from Bed 6; (D) mudstone strata intruded by gabbro nearly along the bedding directions; (E-F) thick-bedded litharenite strata from Bed 7; (G) grayish black mudstones with horizontal beddings; (H) Ordovician Baota Formation limestone strata with abundant cameroceras fossils.

CO_2 and to determine carbon and oxygen isotopic compositions. The samples are cleaned and selected to exclude the influence of diagenesis. The selected carbonate rocks are crushed to 200 mesh before reacting with supersaturated phosphoric acid. The generated CO_2 was tested with a MAT253 stable isotope mass spectrometer. The carbon isotope values are expressed by $\delta^{13}C_{V\text{-}PDB}$. The error range is controlled within 0.1 ‰.

4.5. Detrital zircon U-Pb dating and in-situ trace element measurement

The detrital zircon grains were firstly separated from fresh samples using density and magnetic techniques, were carefully hand-picked under a binocular microscope and then were mounted in epoxy resin. These zircon grains were polished to expose the internal texture. Cathode luminescence (CL) images of all the mounted zircon grains were obtained. The zircon U-Pb isotopic and trace elemental compositions of six samples were performed on a LA-ICP-MS (combing a NWR 193 laser system & an Agilent 7900 mass spec) at the Mineral Laser Microprobe Analysis Laboratory (Milma Lab), China University of Geosciences, Beijing (CUGB), China. About 60–120 zircon grains were analyzed for each sample. Zircon standards 91,500 (1065 Ma) and GJ-1 (607 Ma) and the NIST SRM 610 glass were simultaneously measured for analytical quality control. The measured compositions were corrected for common Pb using measured ^{204}Pb. Zircon U-Pb ages with poor precision and high discordance were omitted from the kernel density estimation plots and from interpretation. Ages <1000 Ma were based on common Pb corrected $^{206}Pb/^{238}U$ ratios, whereas ages >1000 Ma were based on common Pb corrected $^{206}Pb/^{207}Pb$ ratios.

4.6. Detrital zircon Lu-Hf isotopic analysis

A total of 116 detrital zircon grains from three dated sandstone samples were measured for Hf isotopes after U-Pb dating, using a LA-

MC-ICP-MS. The zircon standards GJ-1, Plesovice and Mud Tank was analyzed for monitoring the measurement quality. The obtained $^{176}Lu/^{177}Hf$, $^{176}Hf/^{177}Hf$ ratios and the ^{176}Lu decay constant of 1.867×10^{-11} $year^{-1}$ were applied to calculate initial $^{176}Hf/^{177}Hf$ ratios. The $\varepsilon_{Hf}(t)$ values were calculated using 0.0336 and 0.282785 as the $^{176}Lu/^{177}Hf$ and $^{176}Hf/^{177}Hf$ ratios for the chondritic uniform reservoir (Wu et al., 2007; Bouvier et al., 2008), respectively. Detailed Hf isotopic analysis methods were given by Li et al. (2018a).

5. Results

5.1. Sandstone framework grain and heavy mineral compositions

The analyzed 14 samples are characterized by poorly-sorted, lithic fragment-rich sandstones (Fig. 7). Most detrital grains therein are angular to subangular in shape (Fig. 7A). These lithic fragments mainly include volcanic fragments and chert grains (Fig. 7B, C, G–I), with subordinate sedimentary fragments and metamorphic fragments. The detrital quartz shows variable grain sizes and some quartz grains have embayed margins (Fig. 7B). Detrital feldspar is dominated by plagioclase and K-feldspar is relatively minor. Some feldspar grains are euhedral and subhedral in shape. The modal analysis results of the framework grain compositions indicate that sandstones from the Qiongzhusi and Canglangpu Formations have Qm-F-Lt (Qm: monocrystalline quartz, F: feldspar and Lt: lithic fragment with chert involved) ratios of 15:22:63 (10 samples) and 19:12:69 (4 samples), respectively. The Canglangpu Formation sandstones have relatively lower volcanic lithic fragment contents and higher chert and metamorphic lithic fragment contents than the Qiongzhusi Formation sandstones (Fig. 8). The framework grain-based Dickinson ternary plots demonstrate that most of the

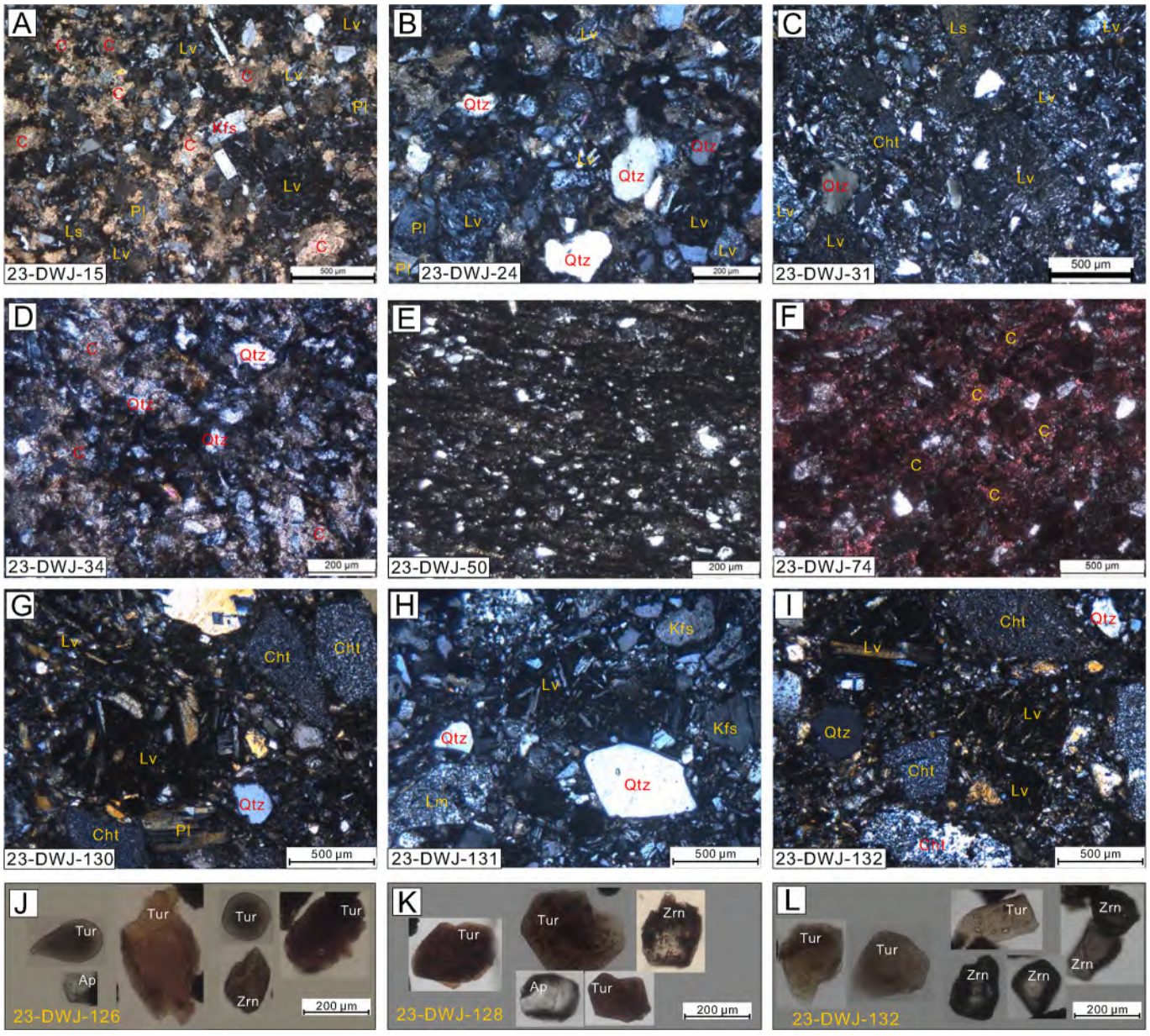

Fig. 7. Representative photomicrographs of the analyzed sample thin-sections and transparent heavy minerals separated from sandstone samples. (A) Carbonate-rich fine-grained litharenite; (B) medium-grained litharenite; (C) coarse-grained litharenite; (D) carbonate-rich siltstone; (E) silty mudstone; (F) sandy limestone (stained with alizarin red solution); (G)-(I) coarse-grained litharenite; (J)-(K) heavy minerals from representative analyzed sandstone samples. Qtz: quartz; Pl: plagioclase; Lv: volcanic lithic fragment; Ls: sedimentary lithic fragment; C: carbonate; Cht: chert; Zrn: zircon; Tur: tourmaline; Ap: apatite. (For interpretation of the references to colour in this figure legend, the reader is referred to the web version of this article.)

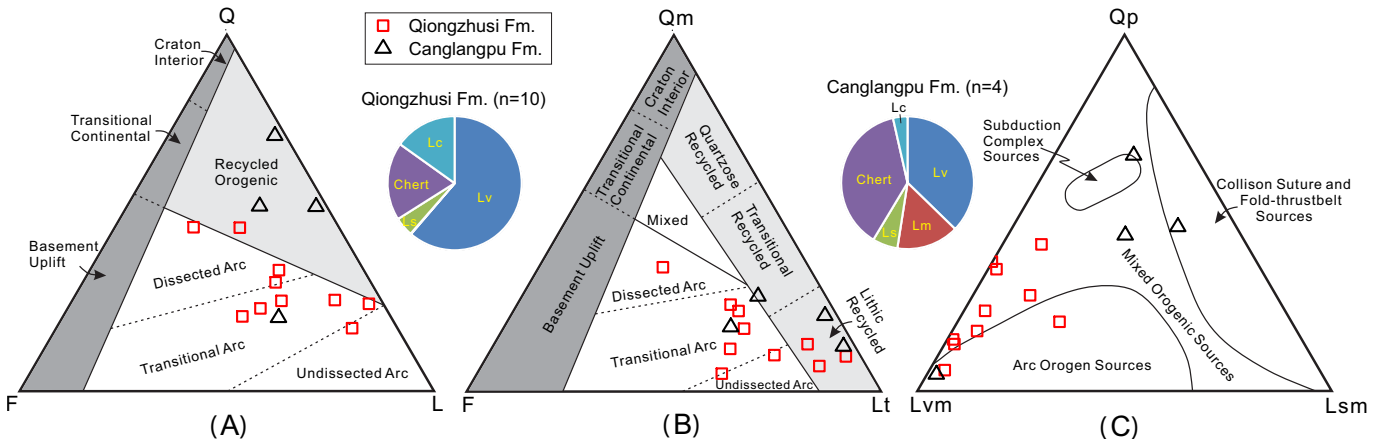

Fig. 8. Modal analysis results of the sandstone framework grain compositions. (A) Q-F-L diagram; (B) Qm-F-Lt diagram; (C) Qp-Lvm-Lsm diagram. The tectonic fields are from Dickinson (1985). The pie charts indicate average data of the lithic fragment compositions. Q: monocrystalline quartz (Qm) and polycrystalline quartz (Qp); F: plagioclase and K-feldspar; L: lithic fragment excluding chert and carbonate fragment; Lt: lithic fragment with chert involved; Lvm: volcanic and meta-volcanic lithic fragment; Lsm: sedimentary and meta-sedimentary lithic fragment (carbonate excluded). Most Maidiping Formation samples are plotted in the arc-related fields, whereas the Canglangpu Formation samples are dominantly in the recycled orogenic fields.

Qiongzhusi Formation sandstones fall into the arc-related fields, whereas the Canglangpu Formation samples mainly fall into the orogenic fields (Fig. 8). All the point-count data of the analyzed samples are shown in Table S1 (see the supplemental data file).

Transparent heavy minerals in the analyzed sandstone samples present low contents and thus the quantitative data are not shown in this contribution. The available heavy mineral grains show variable grain sizes and mainly include tourmaline, zircon, apatite and minor chlorite and titanite. Most of these heavy minerals are angular to subangular with euhedral or subhedral shapes (Fig. 7J–L).

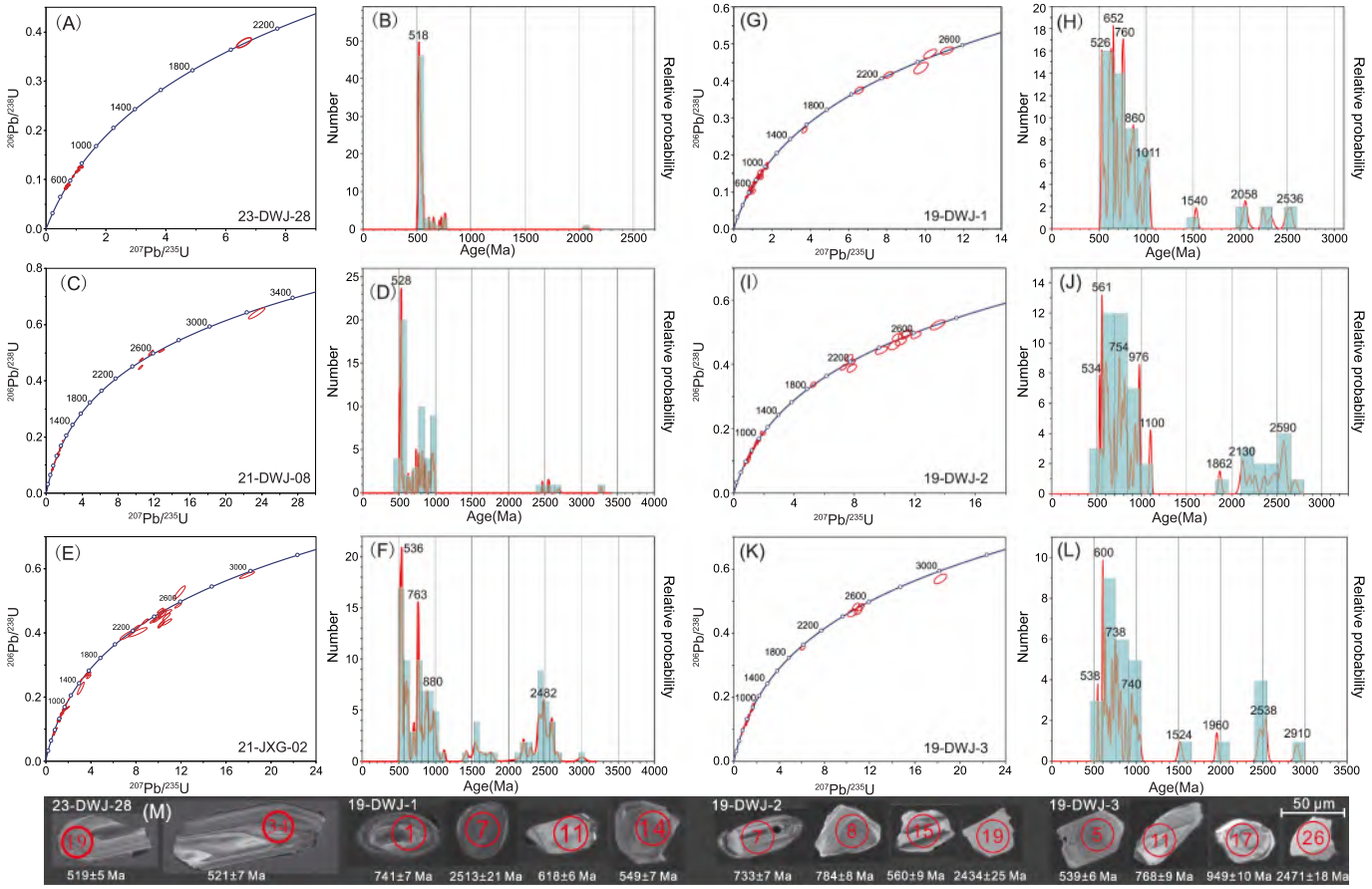

Fig. 9. Detrital zircon U-Pb age data from the six analyzed samples. (A-D) Samples 23-DWJ-28 and 21-DWJ-08 from the Cambrian Qiongzhusi Formation; (E-L) samples 21-JXG-02, 19-DWJ-1, 19-DWJ-2 and 19-DWJ-3 from the Cambrian Canglangpu Formation; (M) representative cathode luminescence images of the analyzed detrital zircon grains.

5.2. Detrital zircon U-Pb ages, trace elemental and Hf isotopic compositions

The detrital zircons of the two Qiongzhusi Formation samples (23-DWJ-28 and 21-DWJ-08) are dominated by latest Neoproterozoic to Cambrian ages (e.g., 560–500 Ma), with age peaks at 518 (Fig. 9A–B) and 528 Ma (Fig. 9C–D), respectively. The sample 21-DWJ-08 therein also shows certain Tonian ages. By contrast, the four Canglangpu Formation samples (19-DWJ-1, 19-DWJ-2, 19-DWJ-3 and 21-JXG-02) display more diverse detrital zircon age populations. The dated detrital zircon grains from sample 21-JXG-02 are dominated by Ediacaran to Cambrian (635–500 Ma, with a predominant age peak at 538 Ma), Tonian (1000–750 Ma) and Neoarchean to Paleoproterozoic (2600–2100 Ma) ages with minor Mesoproterozoic ages (Fig. 9E–F). Samples 19-DWJ-1, 19-DWJ-2 and 19-DWJ-3 have similar detrital zircon U-Pb age populations which are mainly composed of Neoproterozoic to Cambrian ages (1000–520 Ma), with subordinate Neoarchean to Mesoproterozoic ages (Fig. 9G–L). All the raw U-Pb geochronological data are shown in Table S2 (see the supplemental data file). Representative CL images of the dated detrital zircon grains are shown in Fig. 9M and most zircons are characterized by oscillatory zoning textures.

Most dated detrital zircons (424 grains) from the six samples were measured for trace element concentrations. The raw data and representative elemental ratios are shown in Table S3 (see the supplemental data file). The results of detrital zircon grains with ages of 650–500 Ma (data of 181 grains are valid) show that the Nb/Hf and U/Yb ratios range from 0.00007 to 0.00147 and from 0.23 to 22.81, respectively. The $Log_{10}(Sc/Yb)$ and $Log_{10}(Nb/Yb)$ values vary from −0.53 to 2.11 and from −2.77 to −0.79, respectively.

Eleven, sixty-two and forty-three dated zircon grains (mostly having Neoproterozoic and Cambrian U-Pb ages) were selected from samples 19-DWJ-1, 21-DWJ-08 and 23-DWJ-28 for measuring Hf isotopes, respectively. The Hf isotopic ratios and calculating results are shown in Table S4 (see the supplemental data file). Zircons with early-mid Neoproterozoic ages have variable ε_{Hf} (t) values (Fig. 10) with a range of −20 to 12 (averaging at 0.5), whereas the late Neoproterozoic and Cambrian zircon grains present relatively positive $\varepsilon_{Hf}(t)$ values (ranging from −9 to 9, fifty in 68 grains >0, averaging at 1.1). The analyzed Archean to Mesoproterozoic zircon grains also display variable $\varepsilon_{Hf}(t)$ values, with a range of −13 to 23 (Fig. 10; Table S4).

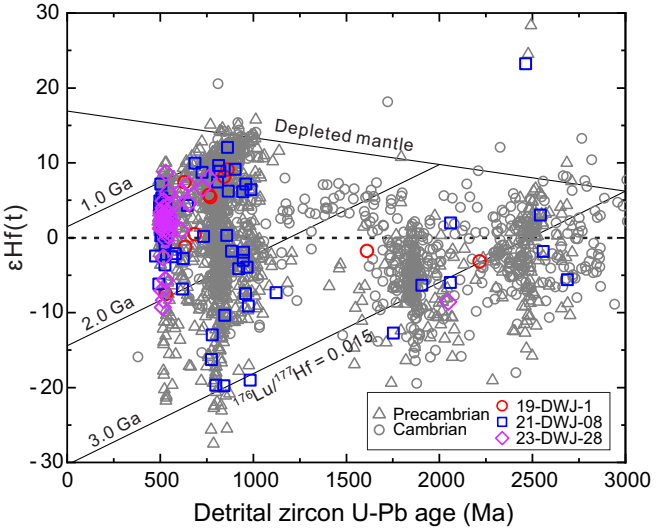

Fig. 10. Representative detrital zircon Hf isotopic data of the dated Cambrian sandstone samples from the Dawuji section and comparison with Hf isotopic data of the Precambrian basement (Jian et al., 2020 and references therein) and previously investigated Cambrian strata (Ye, 2025 and reference therein) in the western-northwestern Yangtze Block. The $\varepsilon_{Hf}(t)$ values were calculated based on equations described by Wu et al. (2007). The raw Hf isotopic data are presented in Table S4 in the supplemental files.

5.3. Whole-rock mineralogical and clay mineralogical compositions

All the whole-rock and clay XRD analysis data are shown in Tables S5 and S6 (in the supplementary data), respectively. The results exhibit that the analyzed 9 samples are mainly composed of quartz, plagioclase and clay minerals, with subordinate K-feldspar and calcite. Pyrite occurs in most samples (Table S5), with relative contents ranging from 3.8 % to 10.9 %. The clay minerals of the analyzed 8 samples are dominated by illite, with minor chlorite. Some samples show relatively high Illite/Smectite mixed layers (Table S6).

5.4. Whole-rock major and trace elemental compositions

The major and trace elemental concentrations of the analyzed 38 samples were normalized to the Upper Continental Crust (UCC) compositions (Fig. 11). Most samples show depletion in Ca, Li, Cs and Sr and enrichment in P, Ba, U and Mo relative to UCC. The binary plots between SiO_2/Al_2O_3 and Fe_2O_3/K_2O demonstrate most samples are plotted in the fields of wacke, shale, arkose and some in the Fe-shale and litharenite fields (Fig. S1 in the supplemental data file). Chondrite-normalized rare earth element (REE) patterns are featured by light REEs enrichment, slightly negative Eu anomaly and flat middle and heavy REEs, while Post-Archean Australian Shale (PAAS)-normalized REE patterns show enrichment in light REEs and slightly positive Eu anomalies (0.72–1.55, 29 in 38 samples have Eu/Eu* >1) for most samples (Fig. S2 in the supplemental data file). In the A-CN-K diagram (Fig. 12A), most samples are plotted close to the plagioclase-K-feldspar line, indicating mild weathering intensity. In the A-CNK-FM ternary diagram (Fig. 12B), the samples are plotted close to the reference point of granodiorite. The calculated Chemical Index of Alteration (CIA) and Index of Compositional Variability (ICV) values (see the figure captions for the calculation formulas) of the analyzed samples have ranges of 40–68 (averaging in 54.5) and 0.7–1.7 (averaging in 0.97) (Fig. 12C), respectively. The representative trace element ratios, La/Th, Th/Sc and Zr/Sc, are variable and are ranging in 1.05–6.07 (averaging in 3.03), 0.36–1.70 (averaging in 0.64) and 7.0–21.3 (averaging in 11.3), respectively. All the raw data are shown in Table S7 in the supplemental data file.

5.5. Carbonate stable carbon isotopes

The $\delta^{13}C_{V\text{-}PDB}$ values of 67 samples from the Qiongzhusi and Canglangpu Formations are generally negative, ranging from −7.6 ‰ to 3.1 ‰ and the $\delta^{13}C_{V\text{-}PDB}$ curve shows two distinct positive shifts as shown in Fig. 3. For the Bed 1 samples (the basal Qiongzhusi Formation), the $\delta^{13}C_{V\text{-}PDB}$ values rise from −4.8 ‰ to 0.1 ‰, then fall back to −6.2 ‰, showing a sharp positive drift. For the Bed 6 samples (the lower Canglangpu Formation), the $\delta^{13}C_{V\text{-}PDB}$ values first decrease from 2.1 ‰ to around 0.1 ‰, then rise to 2.5 ‰, and then rapidly decrease to −5.7 ‰, forming another significant positive drift. The $\delta^{13}C_{V\text{-}PDB}$ values in the upper strata remain relatively negative, rising to 0.5 ‰ shortly and then falling to −2.3 ‰ followed by recovering slightly to near −0.9 ‰. Our obtained geochemical results of whole-rock samples show very weak correlations between $\delta^{13}C_{V\text{-}PDB}$ and $\delta^{18}O_{V\text{-}PDB}$, and very low Mn/Sr and Fe/Sr ratios, indicating very limited diagenesis effect.

6. Discussion

6.1. Depositional ages of the Qiongzhusi and Canglangpu Formations

Detrital zircon U-Pb dating is thought to provide useful information for constraining depositional ages for unknown sedimentary strata in which the biostratigraphy has not been established or that are devoid of

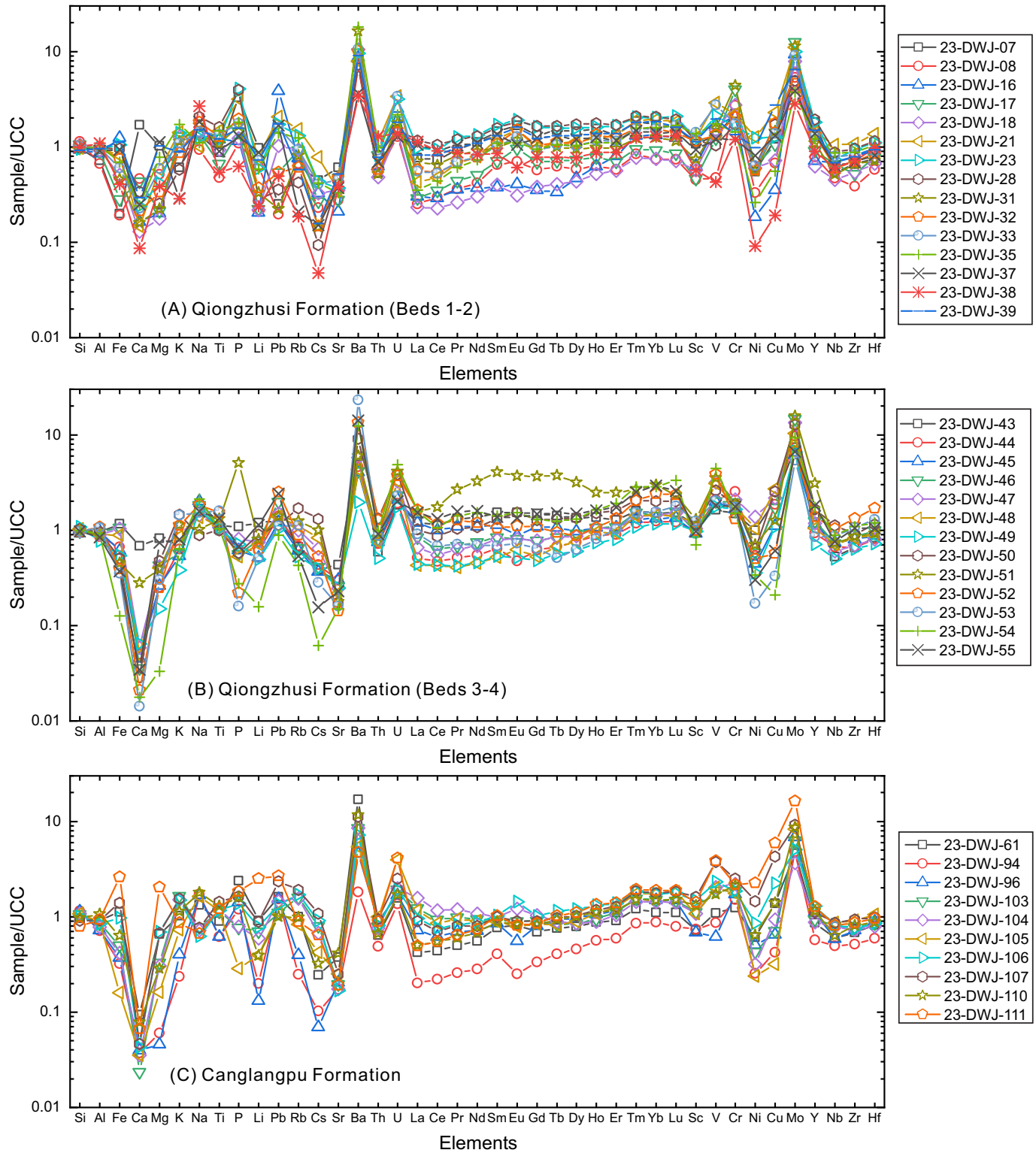

Fig. 11. Upper Continental Crust (UCC) compositions-normalized major and trace element geochemical spider diagrams for all the analyzed samples. The UCC data are from Rudnick and Gao (2014).

volcanic ash interlayers (Gehrels, 2014). And the youngest detrital zircon grains commonly yield the maximum depositional ages, especially in the areas that underwent active volcanism during sediment accumulation (Gehrels, 2014). For the Dawuji section in this study, the U-Pb age spectra of detrital zircons from the lowermost sandstones (Bed 1, Fig. 3) are characterized by a single peak age of ca. 518 Ma (Sample 23-DWJ-28, Fig. 3; Fig. 9A), implying that the sandstone depositional age is less than 518 Ma. On the other hand, the stable carbon isotopic record ($\delta^{13}C$) from the Cambrian has been widely used as constraining and correlating the Cambrian sedimentary successions (Zhu et al., 2006; Chang et al., 2016; Wu et al., 2021b). There are 10 distinct carbon isotopic excursions that can be recognized from the global Cambrian $\delta^{13}C$ reference curve (Fig. 3; Zhu et al., 2019). In our work, we attempted to construct the $\delta^{13}C$ curve for the accessible carbonate rocks and the

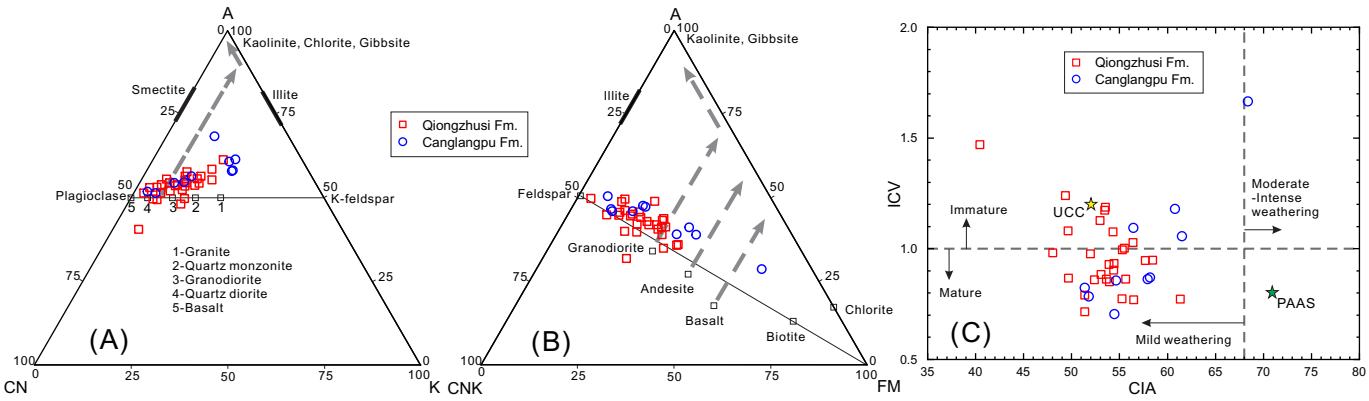

Fig. 12. Chemical weathering intensity and compositional maturity evaluations of the analyzed sedimentary rock samples based on major elemental results. (a) A–CN–K ternary diagram (Al_2O_3-CaO* + Na_2O-K_2O in molecular proportions, modified from Fu et al. (2022)); (b) A-CNK-FM ternary diagram (Al_2O_3-CaO* + Na_2O + K_2O-Fe_2O_3 + MgO in molecular proportions, modified from McLennan et al. (1993)); (C) binary plots between CIA (Chemical Index of Alteration, as the most widely used proxy for quantifying chemical weathering degree) and ICV (Index of Compositional Variability, as a compositional maturity proxy) values. CIA = Al_2O_3 / (Al_2O_3 + K_2O + Na_2O + CaO) × 100 (In the CIA calculation, all variables represent the molar amounts of major-element oxide, and the CaO represents its fraction in silicate minerals only without contributions of CaO from carbonate and phosphate minerals); ICV = (Fe_2O_3 + K_2O + Na_2O + CaO + MgO + MnO + TiO_2) / Al_2O_3. The UCC and PAAS data are from Rudnick and Gao (2014), and Taylor and McLennan (1985), respectively.

new $\delta^{13}C$ data were correlated with the global carbon isotopic curve. For the thick carbonate-rich succession from the Canglangpu Formation (Bed 6, Fig. 3), the lower $\delta^{13}C$ curve shows overall positive values with minor negative shift in the middle, which corresponds well with the global MICE (MIngxinsi Carbon isotope Excursion event) (Zhu et al., 2006, 2019). Thus, we regard the base of the thick Cambrian carbonates as the Age 4 of Epoch 2 (ca. 514.5 Ma). The middle and upper $\delta^{13}C$ curve shows overall negative values from a slightly positive to large negative shift then to minorly negative shift (Fig. 3). This feature can be correlated with the AECE (Archaeocyathid Extinction Carbon isotope Excursion event) from the global carbon isotopic curve (Fig. 3). Meanwhile, the $\delta^{13}C$ curve in the lowermost carbonate rocks (Bed 1) increases upward from a large negative value to a peak value of nearly 0, then decreases continuously to a large negative value. This has the feature between the SHICE (SHIyantou Carbon isotope Excursion event) and CARE (Cambrian Arthropod Radiation isotope Excursion event), which can be correlated with the Age 2 of the Terreneuvian (ca. 524–521 Ma). As discussed above, this is also consistent with the U-Pb ages from the detrital zircons (less than and close to 518 Ma) in the lowermost sandstones, which are located above the analyzed carbonate strata (Fig. 3).

Therefore, we suggest that the measured succession roughly correlates with the Cambrian Age 2 of the Terreneunian to Age 4 of the Epoch 2 interval (ca. 524–509 Ma). Our results are consistent with previously reported Cambrian depositional ages from records in eastern Chongqing, South China, which present 521–509 Ma depositional ages for the Qiongzhusi, Canglangpu and Longwangmiao Formations (Ren et al., 2019). Furthermore, the Cambrian Canglangpu Formation sandstones are unconformably overlain by the Late Ordovician Baota Formation limestones, which have distinct characteristics of lithological and biological records (Figs. 3 and 6H). The depositional period constraint is reinforced by this unconformity boundary. And this unconformity also reveals a major tectonic movement occurred between Cambrian and Ordovician.

6.2. *Depositional processes and sedimentary environments*

The Cambrian sedimentary successions at the Dawuji section are approximately 1000 m in thickness and are characterized by coarsening-upward siliciclastic rocks interlayered with carbonate rocks (Fig. 3). As described above, those black gray thin-bedded mudstone, silty mudstone and calcareous mudstone layers from the Qiongzhusi Formation are rich in pyrite nodules (Figs. 4–5). These nodules are distributed along the bedding directions and thus most likely accumulated during the depositional period (i.e., *syn*-depositional nodules), rather than diagenetic nodules, revealing relatively anoxic, deep-water depositional environments. This is consistent with sedimentary geochemical data that these fine-grained siliciclastic rocks are rich in Mo and U (most samples are plotted close to the Anoxic field in the Mo_{EF}-U_{EF} binary diagram, Fig. 13B). The widespread carbonate slump deposits from the Canglangpu Formation (Figs. 5–6) are of depositional origin, rather than diagenetic origin and reveal relatively high-slope depositional settings. Carbonate slumps in many cases tend to be interpreted as deep-water slope facies due to tectonic (seismic activity or the tectonically induced steepening of slopes) or climatic (such as climate change-induced sea-level oscillations or extreme terrigenous inputs) factors (e.g., Bassant et al., 2005; Dilliard et al., 2010; Mastrogiacomo et al., 2012; Komatsu et al., 2014). Although the mechanism of soft carbonate-rich sediment slumping collapse remains uncertain in this case, the mixed carbonate and siliciclastic features most likely point to deep-water slope-basin environments where gravity flows prevailed (e.g., Dilliard et al., 2010). This interpretation is reinforced by the detrital textures that poorly-sorted detrital grains are dominant in most analyzed sandstones and carbonate-rich sandstones (Fig. 7). The upper Canglangpu Formation is dominated by thick, moderately-sorted sandstone interbedded by thin, gray muddy siltstone and siltstone (Fig. 3), implying increasing detrital inputs. We propose that these terrigenous detritus-dominated successions were most likely deposited in delta front environments. Given the potential high-slope settings without river facies signals, we favor fan delta environments that were close to the source terranes for the upper coarsening-upward detrital records. In summary, the Qiongzhusi Formation accumulated in deep-water basin settings, whereas the Canglangpu Formation documented a change from a mixed slope to fan delta environments with increasing detritus inputs and high sedimentation rates.

Elemental geochemical data of fine-grained siliciclastic rocks also document sedimentary environments and weathering history of the source-to-sink system (e.g., Bennett and Canfield, 2020; Fu et al., 2023). Both the A-CN-K (and the CIA values) and the A-CNK-FM ternary plot results of the analyzed samples reveal mild weathering intensity (Fig. 12). This is not only inconsistent with the early Cambrian records in other places of the western Yangtze Block (most displaying moderate and even intensive weathering intensity, e.g., Zhai et al., 2018; Zhou et al., 2019 and our unpublished data), but also is decoupled with the regional (and global) climate conditions (greenhouse prevailed in the early stage of the early Paleozoic time, e.g., Babcock et al., 2015; Hearing et al., 2018; Goldberg et al., 2021). A reasonable interpretation

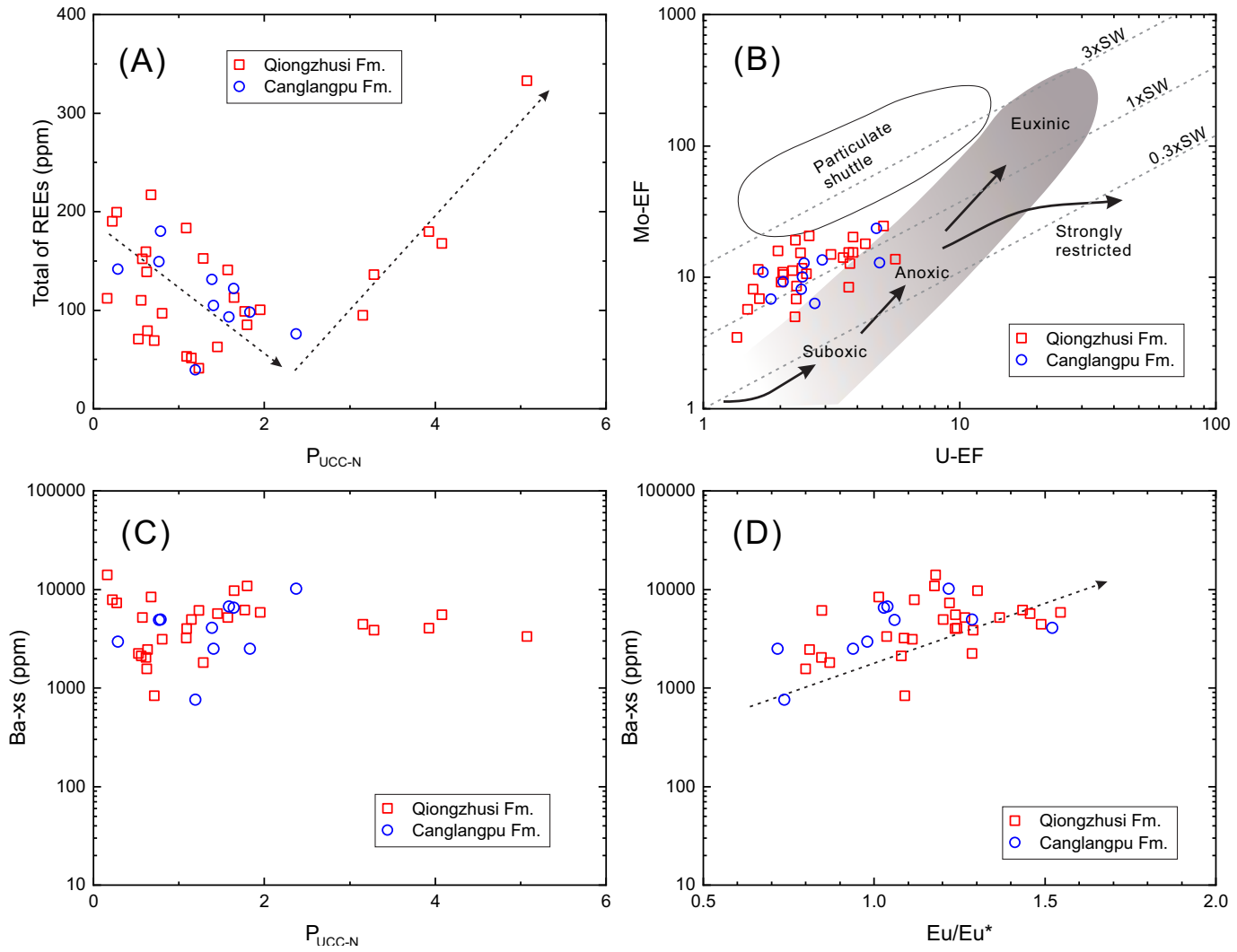

Fig. 13. Representative major and trace elemental proxy data of the analyzed samples for sedimentary environment interpretations. (A) total contents of REEs vs. UCC-normalized P contents (P_{UCC-N}); (B) Mo_{EF} vs. U_{EF}, the diagonal dotted lines represent different Mo:U ratios of modern seawater (indicating 0.3, 1 and 3) (modified from Algeo and Tribovillard (2009)); (C) Ba_{xs} vs. P_{UCC-N}; (D) Ba_{xs} vs. Eu/Eu* (calculated based on PAAS-normalized data). Most samples indicate high P, Mo, U and Ba contents. The Eu/Eu* data ($Eu/Eu^* = Eu_N/(Sm_N \times Gd_N)^{0.5}$) are calculated based on PAAS-normalized data. The enrichment factors (EFs) of elements Mo and U were calculated according to $X_{EF} = (X/Al)_{sample}/(X/Al)_{PAAS}$, where X and Al represent the weight percent values of elements X and Al, respectively. Ba_{xs} represents Excess Ba (assumed to be equivalent to biogenic Ba) and is calculated as total Ba (Ba_{total}) minus detrital Ba, i.e., $Ba_{xs} = Ba_{total} - (Ba/Al)_{detrital} \times Al_{sample}$ (Schoepfer et al., 2015), where $(Ba/Al)_{detrital}$ is for the PAAS composition, and Al_{sample} represents the concentration of element Al in the analyzed samples. In the binary diagram of Mo_{EF} and U_{EF}, the gray field with a gradient ramp represents a "unrestricted marine" depositional system with no limited trace metal renewal. The "particulate shuttle" field indicates a depositional environment where intense redox cycling of metals may occur within the water column (Tribovillard et al., 2012).

is that rapid erosion in sedimentary sources and high sedimentation rates in depositional sinks resulted in a kinetic-limited weathering regime, leading to more source material inheritance and less sediment chemical alteration than those under a supply-limited regime (Fu et al., 2023 and references therein). If the explanation is reasonable, the sediment weathering records at the Dawuji section imply quite active tectonic activities (e.g., uplift and exhumation) in the sedimentary sources. The mild weathering intensity and potentially high erosion rate conditions are also reinforced by the whole-rock mineralogical and clay mineralogical compositions which present high plagioclase contents in the major mineral compositions (Table S5) and high illite contents in the clay mineral assemblages (Table S6).

Furthermore, we suggest that the depositional area was more or less influenced by hydrothermal activities. This can be explained as follows. Most samples display positive Eu anomalies (i.e., Eu/Eu* >1, as a hydrothermal environment proxy, Bau (1991)) according to the PAAS-normalized data (Fig. 13D). Although many samples have relatively high plagioclase contents (Table S5), the positive Eu anomalies based on PAAS-normalized data (Fig. S2) are not due to the occurrence of plagioclase, because the Chondrite-normalized REE patterns show negative Eu anomalies (Fig. S2). The slightly positive Eu anomalies (Eu/Eu* ranges from 1.0 to 1.6, Fig. 13D) may further indicate effect of low-temperature hydrothermal fluids on the sedimentary succession (e.g., Bau et al., 2010; Wang et al., 2024). It is remarkable that the Ba contents show positive correlations with the Eu anomaly values (Fig. 13D) but do not display correlations with P contents (Fig. 13C). This means that the Ba enrichment was most likely due to hydrothermal activities in the basin, rather than high paleo-productivity. We realize that high Ba abundances are widely present in many Cambrian fine-grained sedimentary records in the Yangtze Block and are generally interpreted as a result of hydrothermal inputs (e.g., Li et al., 2015; Zhang et al., 2016; Wang et al., 2020; Cao et al., 2023), but how the hydrothermal system was spatially and temporally distributed and the potential mechanisms deserve more attentions in future studies.

6.3. Sedimentary provenance interpretations

The newly-obtained petrographic, heavy mineral and detrital zircon results of relatively coarse-grained rocks and elemental compositions of fine-grained siliciclastic rocks are applied to interpret provenance for the Cambrian sedimentary records. The Qiongzhusi Formation sandstones are dominated by volcanic lithic fragments (Fig. 7) and are mostly plotted in the arc-related fields in those detrital framework grain ternary diagrams (Fig. 8). The single-mineral grains, such as quartz, feldspar, zircon and apatite, are euhedral-subhedral in shape or represent as embayed grains (Fig. 7). This means that most of the detrital grains are first-cycle detritus and are of volcanic origin. By contrast, the upper Canglangpu Formation sandstones are composed of more variable lithic fragments (Figs. 7–8), including chert, metamorphic lithic fragment, sedimentary lithic fragment as well as volcanic lithic fragments. These sandstones are plotted in the recycled orogenic field (or mixed orogenic source fields) in the Dickinson diagrams (Fig. 8). Therefore, these sediments did not only indicate volcanic contributions but were also derived from recycled sedimentary sources. The diverse clastic compositions (with both first cycle and recycled detritus) are consistent with the major element-based maturity analyses of analyzed fine-grained siliciclastic rocks, which show that some samples have ICV values >1.0 and others have relatively lower ICV values (0.7–1.0) (Fig. 12).

Detrital zircon U-Pb ages are also consistent with the above provenance interpretations. Specifically, the two Qiongzhusi Formation samples (23-DWJ-28 and 21-DWJ-08) are dominated by Cambrian zircon ages with age peaks at 518 Ma and 528 Ma (Fig. 9), respectively, whereas the four Canglangpu Formation samples (21-JGX-02, 19-DWJ-01, 19-DWJ-02 and 19-DWJ-03) show several zircon age populations (Fig. 9), including Ediacaran to Cambrian (635–500 Ma), Tonian (1000–750 Ma), Neoarchean to Paleoproterozoic (2600–2100 Ma) ages and minor Mesoproterozoic ages (e.g., 1600–1500 Ma). This reveals the Canglangpu Formation sandstones were fed by more complicated, various sources, compared with the Qiongzhusi Formation. The dominant positive $\varepsilon_{Hf}(t)$ values (Fig. 10) also support contributions of arc-related rocks with minor crustal reworking. The widespread Cambrian orogenic signals (i.e., ca. 530–520 zircon ages) were also found from other Cambrian outcrops in the Longmenshan region in previous studies (Fig. 14; Chen et al., 2018, 2021; Gu et al., 2023b; Han et al., 2024; Wang et al., 2025). Some investigations inferred that these zircons were possibly derived from distant orogens, such as the Cadomian arc belt in the Iran-Turkey terranes (Chen et al., 2018, 2021). However, the similarity of Precambrian zircon U-Pb ages and Hf isotopic signatures between western Yangtze Block basements and Cambrian sedimentary records (Fig. 10; Fig. 14) as well as the newly-found early Cambrian arc-related volcanic rocks in this region (Deng et al., 2025), suggest that both Cambrian and Precambrian detrital zircon grains might not need to come from distant sources. More importantly, the first-cycle detritus features and the volcanic materials- and chert-mixed sedimentary records reveal nearby sources. Therefore, we favor an adjacent arc orogenic belt in the northwest contributed major sediments to the study area. Our limited paleocurrent data (unpublished) from a Cambrian outcrop close to the Dawuji section show southeast-directed paleocurrents.

The elements-based provenance indicators are variable (Fig. 15), but present intermediate parent-rocks or mixed acid and mafic rocks for the sediments. Volcanic lithic fragments in the analyzed samples mostly have microlitic and lathwork textural features (Fig. 7), generally interpreted as intermediate volcanic petrofacies (e.g., Affolter and Ingersoll, 2019; Critelli et al., 2023). Furthermore, the patterns of REEs are also consistent with the parent-rock interpretations (Fig. S2). The upward increasing chert and metamorphic lithic fragments in the sandstones reveal exposure and enhanced recycling of chert-rich strata and Precambrian metamorphic basement to the northwest. We note that chert deposits widely accumulated in the Yangtze Block in the Ediacaran and Cambrian periods (e.g., Wang et al., 2012; Zhang et al., 2020; Li et al., 2022; Wang et al., 2022), especially during the Ediacaran–Cambrian transition and most chert records are distributed in central, south and east regions of the Yangtze Block. Recent investigations in the western Yangtze Block, Bikou terrane and West Qinling orogen demonstrated that cherts were also widely deposited in these periods (Gu et al., 2023a, 2025). Our new findings, from the Cambrian sandstone petrography perspective, verify that the western Yangtze Block and the surrounding regions (i.e., the potential source regions for the Cambrian Dawuji section) to the west most likely had similar chert-related sedimentary environments with those mentioned in the literatures (e.g., Wang et al., 2012; Zhang et al., 2020; Li et al., 2022; Wang et al., 2022) during the Ediacaran and earliest Cambrian periods. Further detailed chert fragment explanation is expected to have important implications for better understanding of the Ediacaran and Cambrian paleogeography in the Yangtze Block.

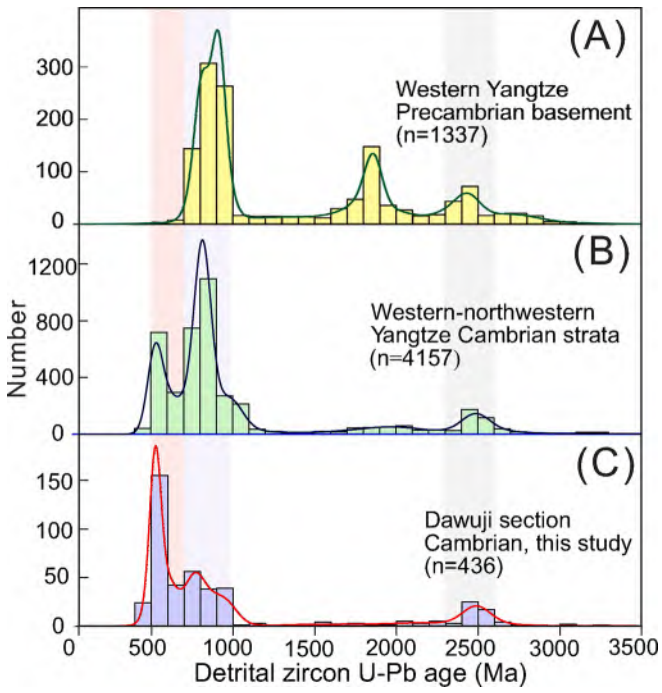

Fig. 14. Comparison of detrital zircon U-Pb age signatures among (A) the Precambrian basement in the western Yangtze Block, (B) previously investigated Cambrian strata in the western-northwestern Yangtze block and (C) newly investigated Cambrian strata (data from 6 samples are combined) at the Dawuji section. The Precambrian basement data are from Jian et al. (2020) and references therein. The reported Cambrian strata data are from Ye (2025) and reference therein.

6.4. Tectonic implications

We favor that the variations in sedimentary environments and provenance are dominantly due to tectonic forcings, rather than climate and sea-level fluctuations. The sea-level rise during the Cambrian (Miller et al., 2005; Haq and Schutter, 2008) may results in upward-fining sedimentary sequences, which is inconsistent with the early Cambrian records at the Dawuji section. As mentioned above, the Cambrian sedimentary successions show a coarsening-upward feature from shale to sandstone, being consistent with an orogen advance. Although the early Cambrian greenhouse climate (Babcock et al., 2015; Hearing et al., 2018) may lead to enhancement of precipitation, runoff and terrigenous sediment fluxes, and thus influenced the sedimentary environments, regional climatic fluctuations hardly altered signals of the source terranes. Previous investigations suggested that the thick Cambrian successions were fed by distal continents due to the assembly and collision of Gondwana (Duan et al., 2011; Chen et al., 2016, 2018; Yang et al.,

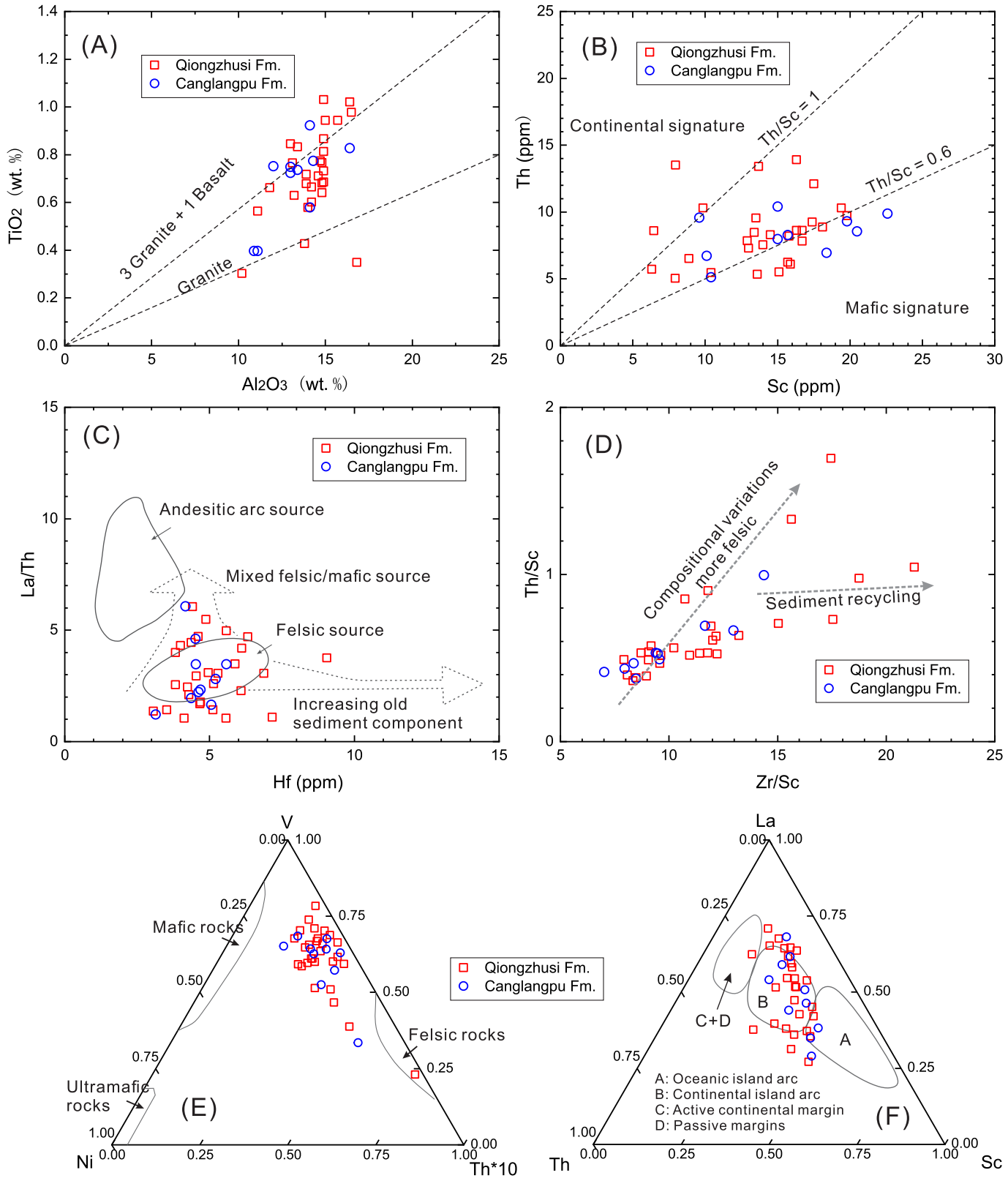

Fig. 15. Sedimentary parent-rock interpretations based on binary or ternary plots by major and trace element geochemical data of the analyzed samples. (A) TiO_2 vs. Al_2O_3 (modified from Schieber (1992)); (B) Th vs. Sc (modified from Totten et al. (2000)); (C) La/Th vs. Hf (after Floyd and Leveridge, 1987); (D) Th/Sc vs. Zr/Sc (after McLennan et al. (1993)); (E) The V–Ni–Th*10 ternary plots (after Bracciali et al. (2007)); (F) La-Th-Sc ternary diagram (after Bhatia and Crook (1986)).

2020; Han et al., 2024). However, Gu et al. (2023b) put forward that the Cambrian clastic sediments were from proximal sources owing to the subduction of the Proto-Tethys Ocean underneath the NW Yangtze Block. In this contribution, several lines of evidence confirm the proposition.

The plots for major elements SiO_2 vs. K_2O/Na_2O and K_2O/Na_2O vs. SiO_2/Al_2O_3 (Fig. S3 in the supplemental data file) all point to the continental arc setting. The trace element discriminant plots, such as La-Th-Sc, Th-Sc-Zr/10, and Th-Zr/10-Co (Fig. 15F; Fig. S4 in the supplemental data file), also denote the continental arc setting. All of these elemental geochemical data indicate that the clastic sediments were shed from nearby continental arcs and older terranes.

Detrital zircon U-Pb age spectra are thought to reflect the tectonic setting of the basin in which sediments are deposited (Cawood et al., 2012). Specifically, convergent plate margins are generally characterized by a large proportion of zircon ages close to the depositional ages of the sediments, whereas sedimentary records in collisional, extensional and intracratonic settings may contain greater proportions with older ages that reflect the history of the underlying basement (Cawood et al., 2012). The age spectra from the Qiongzhusi Formation (samples 23-DWJ-8 and 21-DWJ-08) present a distinctive feature of a single age peak close to the depositional period, which may reveal an active margin setting. The detrital zircon age cumulative proportion curves based on differences between the crystallization and depositional ages (Fig. 16) reveal that the Cambrian sedimentary successions in NW Yangtze Block were most likely under convergent (for the Qiongzhusi Formation) and then collisional (for the Canglangpu Formation) settings. This is reinforced by the sandstone petrographic analyses, which show that the Qiongzhusi Formation sandstones (mainly plotted in arc-related fields in the Dickinson ternary diagram) are dominated by volcanic lithic fragments, whereas the overlying Canglangpu Formation sandstones (mainly plotted in orogenic fields) are composed of various detritus including chert, volcanic and metamorphic lithic fragments (Figs. 7–8). The variations in petrographic compositions reflect increasing contributions from the underlying basement from the depositional period of the Qiongzhusi Formation to that of the Canglangpu Formation. In addition, from the zircon trace elements-based discrimination diagrams (Fig. 17), the detrital zircons with ages ranging from 635 to 500 Ma are plotted within the continental arc field, supporting the active margin settings. Furthermore, previous detrital zircon U-Pb geochronology and sedimentary geochemical results from the Longzikou section (early Cambrian records, ca. 100 km northeast of the Dawuji section, Fig. 1B) in the Longmenshan region also demonstrate proximal arc-related source signals (Gu et al., 2023b), implying that the sediment supply from the early Cambrian arc terrane was a regional event in the NW Yangtze Block, rather than a local event.

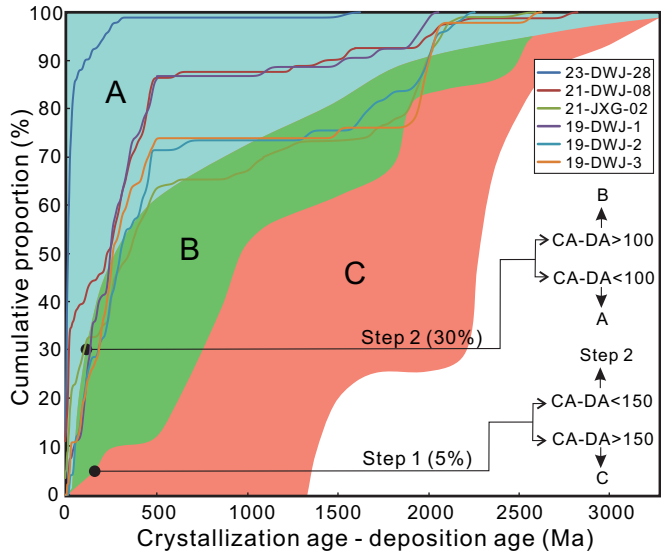

Fig. 16. Age cumulative proportion curves, based on differences between the crystallization and depositional ages (CA-DA) of the detrital zircons of the analyzed six sedimentary rock samples, are regarded as a function of three main tectonic settings (after Cawood et al., 2012). Extensional (including intracratonic) settings are suggested to have CA-DA greater than 150 Ma in the youngest 5 % of the zircons (step 1), and all convergent settings have CA-DA less than 100 Ma in the youngest 30 % of zircons (step 2). A, B and C fields refer to convergent, collisional and extensional basins, respectively (Cawood et al., 2012). As mentioned in the text, the investigated sedimentary successions most likely accumulated during the Age 2 of the Terreneunian to Age 4 of the Epoch 2 (ca. 524–509 Ma) and the depositional age of the lowermost (i.e., the oldest) sandstone sample (i.e., Sample 23-DWJ-28, Fig. 3; Fig. 9A) is less than 518 Ma. Here, depositional ages (DA) of the analyzed samples 23-DWJ-28, 21-DWJ-08 and other four Canglangpu Formation samples were roughly set as 516 Ma, 515 Ma, 509 Ma for calculations, respectively.

It is well known that subduction-related convergent plate margins are also characterized by extensive arc volcanic rocks and metamorphic rocks. Gu et al. (2023b) reported early Cambrian volcanic rocks (ca. 526 Ma, more than hundreds of meters thick) at the Maoxian section (Fig. 1B), 30 km west of the Dawuji section, in the central Longmenshan fold-thrust belt, implying an early Cambrian magmatic event. Recently, Deng et al. (2025) performed detail research for this section, and proposed that the volcanic rocks are shoshonite series consisting of trachyte, trachy-andesite, andesite, dacite, and rhyodacite. These volcanic rocks have crystallization ages ranging from 528 Ma to 523 Ma, have positive zircon $\varepsilon_{Hf}(t)$ values and were interpreted as arc magmatism products associated with subduction-collision in an active continental margin (Deng et al., 2025). This new clue provides important evidence for the proposition of the early Cambrian active margin setting in the NW Yangtze Block. While other early Cambrian arc-related magmatic and metamorphic rock associations have been rarely discovered in the NW Yangtze Block, early Cambrian arc volcanic rocks and ophiolites (ca. 534–514 Ma) were widely found along the Wushan, Tianshui and Sangdan sutures in the Qinling orogen, which were regarded as products of the Proto-Tethys Ocean subduction (Dong and Santosh, 2016; Yang et al., 2018). We note that the Longmenshan fold–thrust belt, the Bikou terrane and the West Qinling orogen (Fig. 1B) are thought to be closely related to the Yangtze Block during that time (Gu et al., 2023b and references therein). However, whether these magmatic arcs served as the sources for the lower Cambrian sediments in the Longmenshan region requires further studies. Although the basement of the thick Triassic flysch complex in the Songpan-Ganzi terrane remains mysterious (Jian et al., 2019 and references therein), several research groups contended that continental basement beneath the eastern Songpan-Ganzi terrane was most likely a continuation of the Yangtze Block (Roger et al., 2004; Zhang et al., 2006; Wang et al., 2007; Yuan et al., 2010; Xu et al., 2015). If this is reasonable, the regions that were covered by the Triassic flysch in the Songpan-Ganzi terrane might be a potential area to find the early Cambrian arc-related volcanic and metamorphic rocks.

A growing number of studies suggest that the South China Craton and other Asian continental fragments (e.g., Tarim, North China, Qiangtang, Lhasa and Sibumasu and Indochina) were located along the northern Gondwana margin in the earliest Paleozoic, were involved in the subduction-closing process of the Proto-Tethys Ocean, and subsequently accreted to East Gondwana (Cawood et al., 2013; Cawood et al., 2018; Zhao et al., 2018; Nouri et al., 2021; Allen et al., 2023), forming a peripheral orogen to the north, named as the North Indo-Australie Orogen (Cawood et al., 2021). Therefore, we suggest that the newly-identified continental arcs were most likely formed in response to the subduction of the Proto-Tethys Ocean underneath the NW Yangtze Block during the assembly process of Gondwana. These results and explanations also demonstrate that the NW Yangtze Block underwent a major tectonic transition from a passive margin to an active margin from the Ediacaran to the Cambrian. Our findings are an important step towards a

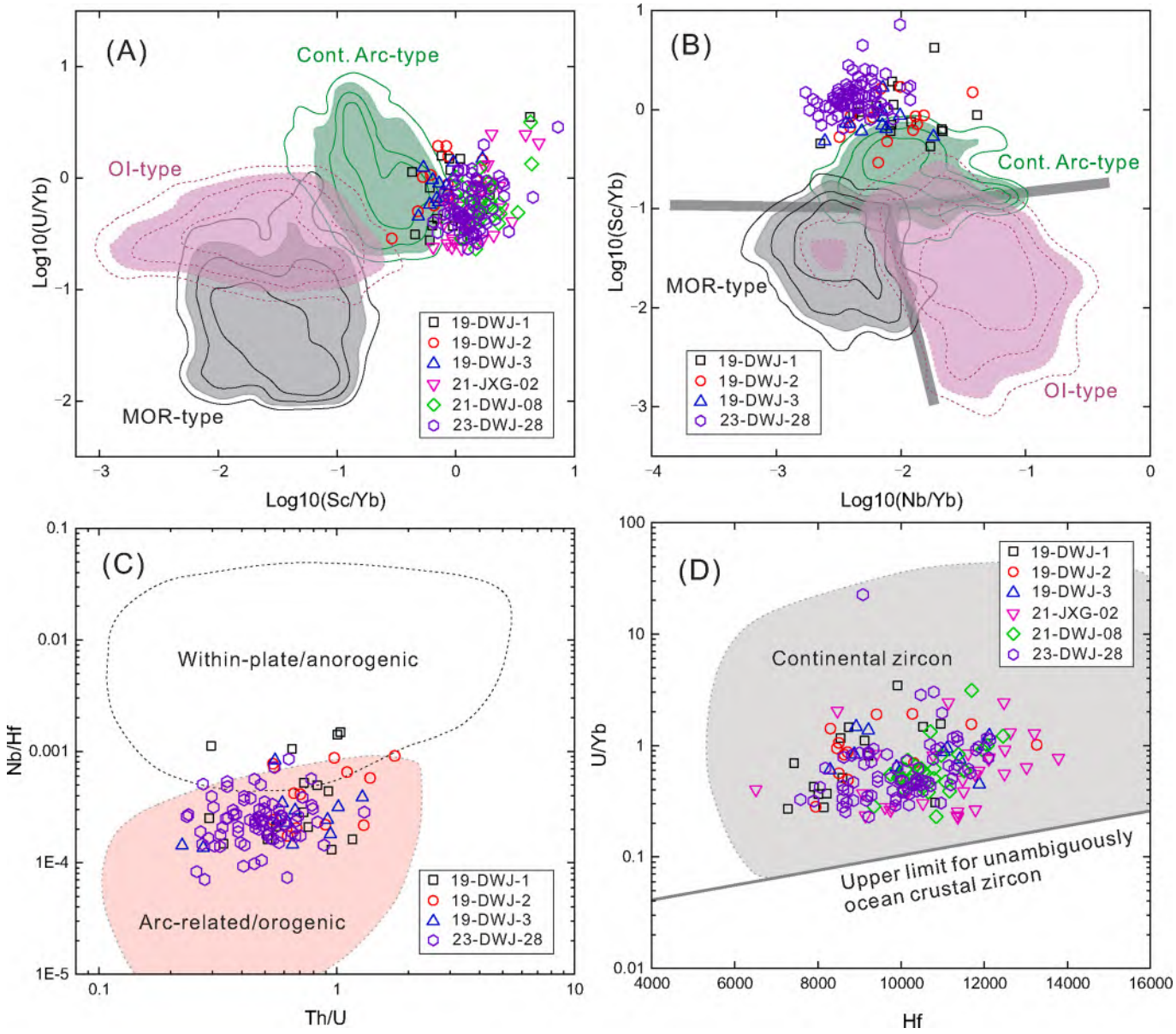

Fig. 17. Representative trace element data of the dated late Neoproterozoic-Cambrian detrital zircon grains (with ages ranging 500–650 Ma) from the Cambrian samples. (A) $Log_{10}(U/Yb)$ vs. $Log_{10}(Sc/Yb)$; (B) $Log_{10}(Sc/Yb)$ vs. $Log_{10}(Nb/Yb)$; (C) Nb/Hf vs. Th/U; (D) U/Yb vs. Hf. The fields indicated in A-B are density distribution plots from Grimes et al. (2015). The contours shown are for 50, 80, 90, and 95 % levels. MOR-type: mid-ocean ridge setting; OI-type: ocean-island setting; Cont. Arc-type: continental arc setting. The fields indicated in C-D are from Yang et al. (2012) and Grimes et al. (2007), respectively.

better understanding of the Cambrian orogeny and the role of the South China in the Gondwana assembly process.

7. Conclusions

In this study, we present comprehensive research results for the Cambrian sedimentary successions from the central Longmenshan region in the NW Yangtze Block, South China. The carbonate stable carbon isotopic data, compared with the global Cambrian $\delta^{13}C$ curve and combined with the maximum depositional age constrain from detrital zircon U-Pb ages, reveal that the investigated successions roughly correlate with the Cambrian Age 2 of the Terreneuvian to Age 4 of the Epoch 2 (ca. 524–509 Ma). Sandstone petrographic results exhibit dominant arc-related orogen sources with upward-increasing recycled orogenic material contributions. The geochemical data of fine-grained siliciclastic rocks demonstrate that these sediments have relatively low maturity and are dominated by first-cycle, intermediate rocks-contributed detritus. Detrital zircon U-Pb ages show predominant Cambrian orogen signals (ca. 530–520 Ma). These zircon ages are close to the inferred depositional ages, also implying an active margin setting for the study area. Furthermore, the trace elements of the zircon grains with ages of 635–500 Ma denote a continental arc origin. All the new data point to dominantly nearby arc-related source terranes for the Cambrian clastic sediments, rather than distant orogen sources as previously proposed. We suggest that the early Cambrian sedimentary system was controlled by subduction-collision processes and the underestimated arc terranes were developed in response to the Proto-Tethys Ocean subduction beneath the NW Yangtze Block. These new findings are important to better understand the Ediacaran–Cambrian transition and the Gondwana assembly process.

CRediT authorship contribution statement

Zhidong Gu: Writing – original draft, Resources, Methodology,

Investigation, Funding acquisition, Formal analysis, Data curation, Conceptualization. **Xing Jian:** Writing – original draft, Resources, Methodology, Investigation, Formal analysis, Data curation, Conceptualization. **Xiufen Zhai:** Writing – original draft, Visualization, Methodology, Investigation. **Xiaotian Shen:** Visualization, Investigation, Data curation. **Shuhuai Ye:** Visualization, Investigation, Data curation.

Declaration of competing interest

The authors declare that they have no known competing financial interests or personal relationships that could have appeared to influence the work reported in this paper.

Acknowledgements

This work was supported by the Science and Technology Major Project of PetroChina (No. 2023ZZ0201 and 2023ZZ16), the National Science and Technology Major Project of the Ministry of Science and Technology of China (No. 2016ZX05004005-001), and the Science and Technology Project of RIPED (No. YGJ2023-01). Drs. Guixia Liu and Hua Jiang from RIPED contributed to field work during 2019–2023. Hanjing Fu, Ling Wang and Yuhao Chen from Xiamen University contributed to some field work and sample analyses. We also appreciate the editor and the two reviewers for their constructive comments and suggestions.

Appendix A. Supplementary data

Supplementary data to this article can be found online at https://doi.org/10.1016/j.palaeo.2025.113207.

Data availability

All the data are available in the Supporting Information and are also reposited at the Open Science Framework (https://osf.io/u368f/).

References

Ackerman, L., Zak, J., Zak, K., Pasava, J., Kachlik, V., Hora, J., Veselovsky, F., Hajna, J., 2022. Carbon, oxygen, and strontium isotopic fingerprint in Neoproterozoic to early Cambrian limestones in an active margin setting: a record of local environment or global changes? Precambrian Res. 370, 106538.
Affolter, M.D., Ingersoll, R.V., 2019. Quantitative analysis of volcanic lithic fragments. J. Sediment. Res. 89 (6), 479–486.
Algeo, T.J., Tribovillard, N., 2009. Environmental analysis of paleoceanographic systems based on molybdenum-uranium covariation. Chem. Geol. 268 (3), 211–225.
Allen, M.B., Song, S., Wang, C., Zeng, R., Wen, T., 2023. An oblique subduction model for closure of the Proto-Tethys and Palaeo-Tethys oceans and creation of the Central China Orogenic Belt. Earth Sci. Rev. 240, 104385.
Amthor, J.E., Grotzinger, J.P., Schroder, S., Bowring, S.A., Ramezani, J., Martin, M.W., Matter, A., 2003. Extinction of Cloudina and Namacalathus at the Precambrian-Cambrian boundary in Oman. Geology 31 (5), 431–434.
Babcock, L.E., Peng, S.C., Brett, C.E., Zhu, M.Y., Ahlberg, P., Bevis, M., Robison, R.A., 2015. Global climate, sea level cycles, and biotic events in the Cambrian Period. Palaeoworld 24 (1–2), 5–15.
Bassant, P., Van Buchem, F.S.P., Strasser, A., Görür, N., 2005. The stratigraphic architecture and evolution of the Burdigalian carbonate-siliciclastic sedimentary systems of the Mut Basin, Turkey. Sediment. Geol. 173 (1–4), 187–232.
Bau, M., 1991. Rare-earth element mobility during hydrothermal and metamorphic fluid-rock interaction and the significance of the oxidation state of europium. Chem. Geol. 93 (3–4), 219–230.
Bau, M., Balan, S., Schmidt, K., Koschinsky, A., 2010. Rare earth elements in mussel shells of the Mytilidae family as tracers for hidden and fossil high-temperature hydrothermal systems. Earth Planet. Sci. Lett. 299 (3–4), 310–316.
Bennett, W.W., Canfield, D.E., 2020. Redox-sensitive trace metals as paleoredox proxies: a review and analysis of data from modern sediments. Earth Sci. Rev. 204, 103175.
Bhatia, M.R., Crook, K.A., 1986. Trace element characteristics of graywackes and tectonic setting discrimination of sedimentary basins. Contrib. Mineral. Petrol. 92, 181–193.
Bouvier, A., Vervoort, J.D., Patchett, P.J., 2008. The Lu-Hf and Sm-Nd isotopic composition of CHUR: constraints from unequilibrated chondrites and implications for the bulk composition of terrestrial planets. Earth Planet. Sci. Lett. 273 (1–2), 48–57.
Bracciali, L., Marroni, M., Luca, P., Sergio, R., 2007. Geochemistry and petrography of Western Tethys cretaceous sedimentary covers (Corsica and Northern Apennines): from source areas to configuration of margins. In: Sedimentary Provenance and Petrogenesis: Perspectives from Petrography and Geochemistry. GSA Special Papers.
Burchfiel, B.C., Chen, Z.L., Liu, Y.P., Royden, L.H., 1995. Tectonics of the Longmen Shan and adjacent regions, Central China. Int. Geol. Rev. 37 (8), 661–735.
Cao, H., Wang, Z., Dong, L., Xiao, Y., Hu, L., Chen, F., Wei, K., Chen, C., Song, Z., Wu, L., 2023. Influence of hydrothermal and upwelling events on organic matter accumulation in the gas-bearing lower Cambrian shales of the middle Yangtze Block, South China. Mar. Pet. Geol. 155, 106373.
Cawood, P.A., Hawkesworth, C.J., Dhuime, B., 2012. Detrital zircon record and tectonic setting. Geology 40, 875–878.
Cawood, P.A., Wang, Y.J., Xu, Y.J., Zhao, G.C., 2013. Locating South China in Rodinia and Gondwana: a fragment of greater India lithosphere? Geology 41, 903–906.
Cawood, P.A., Zhao, G.C., Yao, J.L., Wang, W., Xu, Y.J., Wang, Y.J., 2018. Reconstructing South China in Phanerozoic and Precambrian supercontinents. Earth-Sci. Rev. 186, 173–194.
Cawood, P.A., Martin, E.L., Murphy, J.B., Pisarevsky, S.A., 2021. Gondwana's interlinked peripheral orogens. Earth Planet. Sci. Lett. 568, 117057.
Chang, C., Hu, W.X., Fu, Q., Cao, J., Wang, X.L., Yao, S.P., 2016. Characterization of trace elements and carbon isotopes across the Ediacaran-Cambrian boundary in Anhui Province, South China: implications for stratigraphy and paleoenvironment reconstruction. J. Asian Earth Sci. 125, 58–70.
Chang, H.Z., Chu, X.L., Feng, L.J., Huang, J., Chen, Y.L., 2018. Marine redox stratification on the earliest Cambrian (ca. 542–529 Ma) Yangtze platform. Palaeogeogr. Palaeoclimatol. Palaeoecol. 504, 75–85.
Chen, S.F., Wilson, C.J.L., 1996. Emplacement of the Longmen Shan Thrust-Nappe Belt along the eastern margin of the Tibetan Plateau. J. Struct. Geol. 18 (4), 413–430.
Chen, Q., Sun, M., Long, X.P., Zhao, G.C., Yuan, C., 2016. U-Pb ages and Hf isotopic record of zircons from the late Neoproterozoic and Silurian-Devonian sedimentary rocks of the western Yangtze Block: implications for its tectonic evolution and continental affinity. Gondwana Res. 31, 184–199.
Chen, Q., Sun, M., Long, X., Zhao, G., Wang, J., Yu, Y., Yuan, C., 2018. Provenance study for the Paleozoic sedimentary rocks from the West Yangtze Block: Constraint on possible link of South China to the Gondwana supercontinent reconstruction. Precambrian Res. 309, 271–289.
Chen, Q., Zhao, G., Sun, M., 2021. Protracted northward drifting of South China during the assembly of Gondwana: Constraints from the spatial-temporal provenance comparison of Neoproterozoic–Cambrian strata. GSA Bull. 133 (9–10), 1947–1963.
Cocks, L.R.M., Torsvik, T.H., 2013. The dynamic evolution of the Palaeozoic geography of eastern Asia. Earth-Sci. Rev. 117, 40–79.
Critelli, S., Criniti, S., Ingersoll, R.V., Cavazza, W., 2023. Temporal and spatial significance of volcanic particles in sand (stone): implications for provenance and palaeotectonic reconstructions. Geol. Soc. London Spec. Publ. 520.
Deng, Q., Wang, Z.J., Liu, H., Li, S.J., Liu, J.H., Wang, Q.Y., Lin, J.S., Lan, X.W., 2025. Subduction-collision and rapid uplift of the NW Yangtze Block during the Ediacaran-Cambrian transition: new evidence from the shoshonite series. Int. Geol. Rev. 67, 331–351.
Dickinson, W.R., 1985. Interpreting provenance relations from detrital modes of sandstones. In: Provenance of Arenites, pp. 333–361.
Dilliard, K.A., Pope, M.C., Coniglio, M., Hasiotis, S.T., Lieberman, B.S., 2010. Active synsedimentary tectonism on a mixed carbonate-siliciclastic continental margin: third-order sequence stratigraphy of a ramp to basin transition, lower Sekwi Formation, Selwyn Basin, Northwest Territories, Canada. Sedimentology 57 (2), 513–542.
Domeier, M., 2018. Early Paleozoic tectonics of Asia: towards a full-plate model. Geosci. Front. 9, 789–862.
Dong, Y., Santosh, M., 2016. Tectonic architecture and multiple orogeny of the Qinling Orogenic Belt, Central China. Gondwana Res. 29, 1–40.
Dong, Y., Hui, B., Sun, S., He, D., Sun, J., Zhang, F., Cheng, C., Yang, Z., Shi, X., Zang, R., Long, X., Zhang, G., 2024. Neoproterozoic tectonic evolution and proto-basin of the Yangtze Block, China. Earth Sci. Rev. 249, 104669.
Dong, Y., Liu, X., Santosh, M., Zhang, X., Chen, Q., Yang, C., Yang, Z., 2011. Neoproterozoic subduction tectonics of the northwestern Yangtze Block in South China: constrains from zircon U–Pb geochronology and geochemistry of mafic intrusions in the Hannan Massif. Precambrian Res. 189, 66–90.
Duan, L., Meng, Q.R., Zhang, C.L., Liu, X.M., 2011. Tracing the position of the South China block in Gondwana: U–Pb ages and Hf isotopes of Devonian detrital zircons. Gondwana Res. 19, 141–149.
Floyd, P.A., Leveridge, B.E., 1987. Tectonic environment of the Devonian Gramscatho basin, South Cornwall: framework mode and geochemical evidence from turbiditic sandstones. J. Geol. Soc. London 144 (4), 531–542.
Fu, H., Jian, X., Liang, H., Zhang, W., Shen, X., Wang, L., 2022. Tectonic and climatic forcing of chemical weathering intensity in the northeastern Tibetan Plateau since the middle Miocene. Catena 208, 105785.
Fu, H., Jian, X., Pan, H., 2023. Bias in sediment chemical weathering intensity evaluation: a numerical simulation study. Earth Sci. Rev. 246, 104574.
Gao, P., Liu, G.D., Jia, C.Z., Young, A., Wang, Z.C., Wang, T.S., Zhang, P.W., Wang, D.P., 2016. Redox variations and organic matter accumulation on the Yangtze carbonate platform during Late Ediacaran–Early Cambrian: Constraints from petrology and geochemistry. Palaeogeogr. Palaeoclimatol. Palaeoecol. 450, 91–110.
Gehrels, G., 2014. Detrital zircon U-Pb geochronology applied to tectonics. Annu. Rev. Earth Planet. Sci. 42, 127–149.
Goldberg, S.L., Present, T.M., Finnegan, S., Bergmann, K.D., 2021. A high-resolution record of early Paleozoic climate. Proc. Natl. Acad. Sci. USA 118 (6), e2013083118.

Grimes, C.B., John, B.E., Kelemen, P.B., Mazdab, F.K., Wooden, J.L., Cheadle, M.J., Hanghøj, K., Schwartz, J.J., 2007. Trace element chemistry of zircons from oceanic crust: a method for distinguishing detrital zircon provenance. Geology 35 (7), 643–646.
Grimes, C.B., Wooden, J.L., Cheadle, M.J., John, B.E., 2015. "Fingerprinting" tectono-magmatic provenance using trace elements in igneous zircon. Contrib. Mineral. Petrol. 170, 1–26.
Grotzinger, J.P., Bowring, S.A., Saylor, B.Z., Kaufman, A.J., 1995. Biostratigraphic and geochronologic constraints on early animal evolution. Science 270, 598–604.
Gu, Z.D., Yin, J.F., Jiang, H., Zhang, B., Li, Q., Yuan, M., Zhai, X., Zhang, L., Yang, F., 2016. Tectonic evolution from late Sinian to early Paleozoic and natural gas exploration in northwestern Sichuan Basin, SW China. Pet. Explor. Dev. 43 (1), 1–12.
Gu, Z.D., Lonergan, L., Zhai, X.F., Zhang, B.M., Lu, W.H., 2021. The formation of the Sichuan Basin, South China, during the late Ediacaran to early Cambrian. Basin Res. 33, 12559.
Gu, Z.D., Jian, X., Liu, G., Shen, X., Fu, H., Zhai, X., Jiang, H., 2023a. Age, provenance and tectonic setting of the Tonian–Cryogenian clastic successions in the northwest Bikou terrane, NW Yangtze Block, Central China. Precambrian Res. 397, 107197.
Gu, Z.D., Jian, X., Watts, A.B., Zhai, X., Liu, G., Jiang, H., 2023b. Formation and evolution of an early Cambrian foreland basin in the NW Yangtze Block, South China. J. Geol. Soc. Lond. 180 (3), jgs2022-127.
Gu, Z., Jiang, H., Fu, L., Zhang, B., Zhai, X., Liu, G., Li, Q., 2023c. Ediacaran stratigraphy and paleogeography in the North Yangtze block, South China. Sediment. Geol. 444, 106314.
Gu, Z.D., Jian, X., Liu, G., Fu, H., Shen, X., Zhai, X., Jiang, H., 2025. The Tonian sedimentary records in the southwestern West Qinling orogen, Central China, reveal an active margin setting. Precambrian Res. 418, 107692.
Guo, Q.J., Strauss, H., Zhu, M.Y., Zhang, J.M., Yang, X.L., Lu, M., Zhao, F.C., 2013. High resolution organic carbon isotope stratigraphy from a slope to basinal setting on the Yangtze Platform, South China: implications for the Ediacaran–Cambrian transition. Precambrian Res. 225, 209–217.
Han, Y., Ran, B., Santosh, M., Liu, S., Li, Z., Ye, Y., Lv, F., Wang, H., Li, C., 2024. The Cambrian collision of the Yangtze Block with Gondwana: evidence from provenance analyses. Geol. Soc. Am. Bull. https://doi.org/10.1130/B37470.1.
Haq, B.U., Schutter, S.R., 2008. A chronology of Paleozoic sea-level changes. Science 322 (5898), 64–68.
He, T.C., Zhu, M.Y., Mills, B.J.W., Wynn, P.M., Zhuravlev, A.Y., Tostevin, R., Strandmann, P.A.E.P., Yang, A.H., Poulton, S.W.P., Shields, G.A., 2019. Possible links between extreme oxygen perturbations and the Cambrian radiation of animals. Nat. Geosci. 12 (6), 468–474.
Hearing, T.W., Harvey, T.H., Williams, M., Leng, M.J., Lamb, A.L., Wilby, P.R., Babbott, S.E., Pohl, A., Donnadieu, Y., 2018. An early Cambrian greenhouse climate. Sci. Adv. 4 (5), eaar5690.
Hui, B., Dong, Y., Zhang, F., Sun, S., He, S., 2021. Neoproterozoic active margin in the northwestern Yangtze Block, South China: new clues from detrital zircon U–Pb geochronology and geochemistry of sedimentary rocks from the Hengdan Group. Geol. Mag. 158, 842–858.
Hui, B., Dong, Y., Zhang, F., Sun, S., Neubauer, F., He, D., He, S., 2022. Geochronology, geochemistry, and isotopic composition of the early Neoproterozoic granitoids in the Bikou Terrane along the northwestern margin of the Yangtze Block, South China: petrogenesis and tectonic implications. Precambrian Res. 377, 106724.
Hui, B., Dong, Y., Sun, S., Zhang, F., Zhu, X., Tavakoli, N., Li, Y., Zang, R., 2025. Late Mesoproterozoic passive continental margin in the northwestern Yangtze Block, South China: Insights from the Huodiya Group in the Hannan-Micangshan Massif. Geol. J. 60, 272–289.
Jia, D., Wei, G.Q., Chen, Z.X., Li, B.L., Zeng, Q., Yang, G., 2006. Longmen Shan fold-thrust belt and its relation to the western Sichuan Basin in Central China: new insights from hydrocarbon exploration. AAPG Bull. 90 (9), 1425–1447.
Jian, X., Weislogel, A., Pullen, A., 2019. Triassic sedimentary filling and closure of the eastern paleo-Tethys Ocean: New insights from detrital zircon geochronology of Songpan-Ganzi, Yidun, and west Qinling flysch in eastern Tibet. Tectonics 38, 767–787.
Jian, X., Weislogel, A., Pullen, A., Shang, F., 2020. Formation and evolution of the Eastern Kunlun Range, northern Tibet: evidence from detrital zircon U-Pb geochronology and Hf isotopes. Gondwana Res. 83, 63–79.
Jian, X., Fu, L., Wang, P., Guan, P., Zhang, W., Fu, H., Mei, H., 2023. Sediment provenance of the Lulehe Formation in the Qaidam basin: Insight to initial Cenozoic deposition and deformation in northern Tibetan Plateau. Basin Res. 35, 271–294.
Jian, X., Guan, P., Fu, L., Zhang, W., Shen, X., Fu, H., Wang, L., 2024. Detrital zircon geochronology and provenance of Cenozoic deposits in the Qaidam basin, northern Tibetan plateau: an overview with new data, implications and perspectives. Mar. Pet. Geol. 159, 106566.
Jiang, G.Q., Wang, X.Q., Shi, X.Y., Xiao, S.H., Zhang, S.H., Dong, J., 2012. The origin of decoupled carbonate and organic carbon isotope signatures in the early Cambrian (ca. 542–520 Ma) Yangtze platform. Earth Planet. Sci. Lett. 317-318, 96–110.
Kimura, H., Watanabe, Y., 2001. Oceanic anoxia at the Precambrian-Cambrian boundary. Geology 29 (11), 995–998.
Komatsu, T., Naruse, H., Shigeta, Y., Takashima, R., Maekawa, T., Dang, H.T., Dinh, T., Nguyen, P.D., Nguyen, H.H., Tanaka, G., Sone, M., 2014. Lower Triassic mixed carbonate and siliciclastic setting with Smithian–Spathian anoxic to dysoxic facies, An Chau basin, northeastern Vietnam. Sediment. Geol. 300, 28–48.
Li, Z.W., Liu, S.G., Chen, H.D., Deng, B., Hou, M.C., Wu, W.H., Cao, J.X., 2012. Spatial variation in Meso-Cenozoic exhumation history of the Longmen Shan thrust belt (eastern Tibetan Plateau) and the adjacent western Sichuan basin: constraints from fission track thermochronology. J. Asian Earth Sci. 47, 185–203.
Li, Y., Fan, T., Zhang, J., Zhang, J., Wei, X., Hu, X., Zeng, W., Fu, W., 2015. Geochemical changes in the early Cambrian interval of the Yangtze Platform, South China: implications for hydrothermal influences and paleocean redox conditions. J. Asian Earth Sci. 109, 100–123.
Li, W.P., Zheng, Y.F., Zhao, Y.Y., 2017. Geochemical evidence from marine carbonate for enhanced terrigenous input into seawater during the Ediacaran-Cambrian transition in South China. Precambrian Res. 291, 83–97.
Li, J.Y., Wang, X.L., Gu, Z.D., 2018a. Early Neoproterozoic arc magmatism of the tongmuliang Group on the northwestern margin of the Yangtze block: implications for Rodinia assembly. Precambrian Res. 309, 181–197.
Li, S.Z., Zhao, S.J., Liu, X., Cao, H.H., Yu, S., Li, X.Y., Somerville, I., Yu, S.Y., Suo, Y.H., 2018b. Closure of the Proto-Tethys Ocean and early Paleozoic amalgamation of microcontinental blocks in East Asia. Earth-Sci. Rev. 186, 37–75.
Li, C., Dong, L., Ma, H., Liu, H., Li, C., Pei, H., Shen, B., 2022. Formation of the massive bedded chert and coupled Silicon and Iron cycles during the Ediacaran-Cambrian transition. Earth Planet. Sci. Lett. 594, 117721.
Li, J.Y., Wang, X.L., Cawood, P.A., Gu, Z.D., Guan, Y., 2024a. Neoproterozoic low-T/P metamorphism in the Yangtze Block manifests a long-lived subduction girdle around Rodinia. Earth Planet. Sci. Lett. 634, 118678.
Li, J.Y., Wang, X.L., Gu, Z.D., Wang, D., Du, D.H., 2024b. Geochemical diversity of continental arc basaltic mushy reservoirs driven by reactive melt infiltration. Commun. Earth Environ. 5, 109.
Liu, S., Yang, Y., Deng, B., Zhong, Y., Wen, L., Sun, W., Li, Z., Jansa, L., Li, J., Song, J., Zhang, X., Peng, H., 2021. Tectonic evolution of the Sichuan Basin, Southwest China. Earth Sci. Rev. 213, 103470.
Malusà, M.G., Carter, A., Limoncelli, M., Villa, I.M., Garzanti, E., 2013. Bias in detrital zircon geochronology and thermochronometry. Chem. Geol. 359, 90–107.
Marshall, C.R., 2006. Explaining the Cambrian "Explosion" of animals. Annu. Rev. Earth Planet. Sci. 34, 355–384.
Mastrogiacomo, G., Moretti, M., Owen, G., Spalluto, L., 2012. Tectonic triggering of slump sheets in the Upper cretaceous carbonate succession of the Porto Selvaggio area (Salento peninsula, southern Italy): synsedimentary tectonics in the Apulian Carbonate Platform. Sediment. Geol. 269, 15–27.
McKenzie, N.R., Hughes, N.C., Gill, B.C., Myrow, P.M., 2014. Plate tectonic influences on Neoproterozoic–early Paleozoic climate and animal evolution. Geology 42 (2), 127–130.
McLennan, S.M., Hemming, S., McDaniel, D.K., Hanson, G.N., 1993. Geochemical Approaches to Sedimentation, Provenance, and Tectonics. Special Papers-Geological Society of America, p. 21.
Merdith, A.S., Collins, A.S., Williams, S.E., Pisarevsky, S., Foden, J.D., Archibald, D.B., Blades, M.L., Alessio, B.L., Armistead, S., Plavsa, D., Clark, C., Müller, R.D., 2017. A full-plate global reconstruction of the Neoproterozoic. Gondwana Res. 50, 84–134.
Merdith, A.S., Williams, S.E., Collins, A.S., Tetley, M.G., Mulder, J.A., Blades, M.L., Young, A., Armistead, S., Cannon, J., Zahirovic, S., Müller, R.D., 2021. Extending full-plate tectonic models into deep time: linking the Neoproterozoic and the Phanerozoic. Earth-Sci. Rev. 214, 103477.
Miller, K.G., Kominz, M.A., Browning, J.V., Wright, J.D., Mountain, G.S., Katz, M.E., Sugarman, P.J., Cramer, B.S., Christie-Blick, N., Pekar, S.F., 2005. The Phanerozoic record of global sea-level change. Science 310 (5752), 1293–1298.
Myrow, P.M., Goodge, J.W., Brock, G.A., Betts, M.J., Park, T.S., Hughes, N.C., Gaines, R. R., 2024. Tectonic trigger to the first major extinction of the Phanerozoic: the early Cambrian Sinsk event. Sci. Adv. 10, eadl3452.
Nouri, F., Davoudian, A.R., Allen, M.B., Azizi, H., Asahara, Y., Anma, R., Shabanian, N., Tsuboi, M., Khodami, M., 2021. Early Cambrian highly fractionated granite, Central Iran: evidence for drifting of northern Gondwana and the evolution of the Proto-Tethys Ocean. Precambrian Res. 362, 106291.
Ren, Y., Zhong, D., Gao, C., Li, B., Cao, X., Wang, A., Dong, Y., Yan, T., 2019. The paleoenvironmental evolution of the Cambrian Longwangmiao Formation (stage 4, Toyonian) on the Yangtze Platform, South China: petrographic and geochemical constrains. Mar. Pet. Geol. 100, 391–411.
Roger, F., Malavieille, J., Leloup, P.H., Calassou, S., Xu, Z., 2004. Timing of granite emplacement and cooling in the Songpan–Garzê Fold Belt (eastern Tibetan Plateau) with tectonic implications. J. Asian Earth Sci. 22 (5), 465–481.
Rothman, D.H., Hayes, J.M., Summons, R.E., 2003. Dynamics of the Neoproterozoic carbon cycle. Proc. Natl. Acad. Sci. 100 (4), 8124–8129.
Rudnick, R.L., Gao, S., 2014. The crust. In: Kelemen, P., Hanghøj, K., Greene, A. (Eds.), Treatise on Geochemistry.
Schieber, J., 1992. A combined petrographical—geochemical provenance study of the Newland Formation, mid-Proterozoic of Montana. Geol. Mag. 129 (2), 223–237.
Schoepfer, S.D., Shen, J., Wei, H., Tyson, R.V., Ingall, E., Algeo, T.J., 2015. Total organic carbon, organic phosphorus, and biogenic barium fluxes as proxies for paleomarine productivity. Earth Sci. Rev. 149, 23–52.
Shen, X., Jian, X., Zhang, W., Guan, P., 2024. Grain textural bias in detrital single-mineral provenance studies. Sediment. Geol. 471, 106731.
Shields, G.A., 2007. A normalised seawater strontium isotope curve: possible implications for Neoproterozoic-Cambrian weathering rates and the further oxygenation of the Earth. eEarth 2, 35–42.
Taylor, S.R., McLennan, S.M., 1985. The Continental Crust: Its Composition and Evolution Geoscience Texts, 312. Blackwell Scientific Publications.
Totten, M.W., Hanan, M.A., Weaver, B.L., 2000. Beyond whole-rock geochemistry of shales: the importance of assessing mineralogic controls for revealing tectonic discriminants of multiple sediment sources for the Ouachita Mountain flysch deposits. Geol. Soc. Am. Bull. 112 (7), 1012–1022.
Tribovillard, N., Algeo, T.J., Baudin, F., Riboulleau, A., 2012. Analysis of marine environmental conditions based on molybdenum-uranium covariation applications to Mesozoic paleoceanography. Chem. Geol. 324–325, 46–58.

Wang, C.Y., Han, W.B., Wu, J.P., Lou, H., Chan, W.W., 2007. Crustal structure beneath the eastern margin of the Tibetan Plateau and its tectonic implications. J. Geophys. Res. Solid Earth 112 (B7). https://doi.org/10.1029/2005JB003873.
Wang, J., Chen, D., Wang, D., Yan, D., Zhou, X., Wang, Q., 2012. Petrology and geochemistry of chert on the marginal zone of Yangtze Platform, western Hunan, South China, during the Ediacaran–Cambrian transition. Sedimentology 59 (3), 809–829.
Wang, D., Ling, H.F., Struck, U., Zhu, X.K., Zhu, M.Y., He, T.C., Yang, B., Gamper, A., Shields, G.A., 2018. Coupling of Ocean redox and animal evolution during the Ediacaran-Cambrian transition. Nat. Commun. 9, 2575.
Wang, Z., Tan, J., Boyle, R., Hilton, J., Ma, Z., Wang, W., Lyu, Q., Kang, X., Luo, W., 2020. Evaluating episodic hydrothermal activity in South China during the early Cambrian: Implications for biotic evolution. Mar. Pet. Geol. 117, 104355.
Wang, Z., Xie, X., Wen, Z., 2022. Formation conditions of Ediacaran–Cambrian cherts in South China: Implications for marine redox conditions and paleoecology. Precambrian Res. 383, 106867.
Wang, W., Huang, X., Chen, S., Li, L., Wang, Y., Kang, Y., Nie, Y., 2024. Geochemical characteristics of sediments in the southern Mid-Atlantic Ridge indicate hydrothermal activity: evidence from rare earth elements. Mar. Pet. Geol. 168, 107041.
Wang, Q., Wang, Z., Liu, J., Deng, Q., Liu, H., Li, Z., Zhou, G., Li, S., Xiong, G., Xia, Y., Ma, L., 2025. Depositional sequence and detrital zircon age spectra from Ediacaran to early Cambrian at the northwestern Yangtze craton: implication for the basin dynamics. Precambrian Res. 417, 107667.
Wei, G.Y., Planavsky, N.J., Tarhan, L.G., Chen, X., Wei, W., Li, D., Ling, H.F., 2018. Marine redox fluctuation as a potential trigger for the Cambrian explosion. Geology 46 (7), 587–590.
Wen, H.J., Fan, H.F., Zhang, Y.X., Cloquet, C., Carignan, J., 2015. Reconstruction of early Cambrian Ocean chemistry from Mo isotopes. Geochim. Cosmochim. Acta 164, 1–16.
Wood, R., Liu, A.G., Bowyer, F., Wilby, P.R., Dunn, F.S., Kenchington, C.G., Cuthill, J.F. H., Mitchell, E.G., Penny, A., 2019. Integrated records of environmental change and evolution challenge the Cambrian Explosion. Nat. Ecol. Evol. 3 (4), 528–538.
Wu, F.Y., Li, X.H., Zheng, Y.F., Gao, S., 2007. Lu-Hf isotopic systematics and their applications in petrology. Acta Petrol. Sin. 23 (2), 185–220.
Wu, Y.W., Tian, H., Li, J., Li, T.F., Ji, S., 2021a. Reconstruction of oceanic redox structures during the Ediacaran-Cambrian transition in the Yangtze Block of South China: implications from Mo isotopes and trace elements. Precamrian Res. 359, 106181.
Wu, Y.S., Wang, W., Jiang, H.X., Cui, Y., Zhao, R., Huang, Z.B., Yang, Z.L., Chen, Y.Q., 2021b. Evolution patterns of seawater carbon isotope composition during the Cambrian and their stratigraphic significance. Geol. J. 56 (1), 457–474.
Wu, Y.W., Yin, R.S., Li, C., Chen, D., Grasby, S.E., Li, T.F., Ji, S., Tian, H., Peng, P.A., 2022. Global Hg cycle over Ediacaran–Cambrian transition and its implications for environmental and biological evolution. Earth Planet. Sci. Lett. 587, 117551.
Xie, Y., Li, Y.D., Xiong, X., 2020. Dynamic mechanisms controlling the topography of Longmenshan area. Sci. China Earth Sci. 63, 121–131.
Xu, Y.J., Cawood, P.A., Du, Y.S., Hu, L.S., Yu, W.C., Zhu, Y.H., Li, W.C., 2013. Linking South China to northern Australia and India on the margin of Gondwana: constraints from detrital zircon U-Pb and Hf isotopes in Cambrian strata. Tectonics 32, 1547–1558.
Xu, Y.J., Cawood, P.A., Du, Y.S., Huang, H.W., Wang, X.Y., 2014. Early Paleozoic orogenesis along Gondwana's northern margin constrained by provenance data from South China. Tectonophysics 636, 40–51.
Xu, Z., Dilek, Y., Cao, H., Yang, J., Robinson, P., Ma, C., Li, H., Jolivet, M., Roger, F., Chen, X., 2015. Paleo-Tethyan evolution of Tibet as recorded in the East Cimmerides and West Cathaysides. J. Asian Earth Sci. 105, 320–337.
Xue, Z.H., Martelet, G., Lin, W., Faure, M., Chen, Y., Wei, W., Li, S.J., Wang, Q.C., 2017. Mesozoic crustal thickening of the Longmenshan belt (NE Tibet, China) by imbrication of basement slices: insights from structural analysis, petrofabric and magnetic fabric studies, and gravity modeling. Tectonics 36, 3110–3134.
Yan, Z., Guo, X., Fu, C., Aitchison, J., Wang, Z., Li, J., 2014. Detrital heavy mineral constraints on the Triassic tectonic evolution of the West Qinling terrane, NW China: Implications for understanding subduction of the Paleotethyan Ocean. J. Geol. 122, 591–608.
Yan, D.P., Zhou, Y., Qiu, L., Wells, M.L., Mu, H.X., Xu, C.G., 2018. The Longmenshan tectonic complex and adjacent tectonic units in the eastern margin of the Tibetan Plateau: a review. J. Asian Earth Sci. 164, 33–57.
Yang, J., Cawood, P.A., Du, Y., Huang, H., Huang, H., Tao, P., 2012. Large Igneous Province and magmatic arc sourced Permian–Triassic volcanogenic sediments in China. Sediment. Geol. 261, 120–131.
Yang, L., Song, S., Allen, M.B., Su, L., Dong, J., Wang, C., 2018. Oceanic accretionary belt in the West Qinling Orogen: links between the Qinling and Qilian orogens, China. Gondwana Res. 64, 137–162.
Yang, C., Li, X.H., Li, Z.X., Zhu, M.Y., Lu, K., 2020. Provenance evolution of age-calibrated strata reveals when and how South China Block collided with Gondwana. Geophys. Res. Lett. 47, e2020GL090282.
Ye, S., 2025. Provenance of Cambrian Sandstones in the Northwestern Margin of Yangtze Block and Tectonic Implications. Xiamen University master dissertation. (In Chinese with English abstract).
Yuan, C., Zhou, M.F., Sun, M., Zhao, Y., Wilde, S., Long, X., Yan, D., 2010. Triassic granitoids in the eastern Songpan Ganzi Fold Belt, SW China: magmatic response to geodynamics of the deep lithosphere. Earth Planet. Sci. Lett. 290 (3–4), 481–492.
Zhai, L., Wu, C., Ye, Y., Zhang, S., Wang, Y., 2018. Fluctuations in chemical weathering on the Yangtze Block during the Ediacaran–Cambrian transition: Implications for paleoclimatic conditions and the marine carbon cycle. Palaeogeogr. Palaeoclimatol. Palaeoecol. 490, 280–292.
Zhang, H.F., Zhang, L., Harris, N., Jin, L.L., Yuan, H., 2006. U-Pb zircon ages, geochemical and isotopic compositions of granitoids in Songpan-Garze fold belt, eastern Tibetan Plateau: constraints on petrogenesis and tectonic evolution of the basement. Contrib. Mineral. Petrol. 152, 75–88.
Zhang, J., Fan, T., Algeo, T.J., Li, Y., Zhang, J., 2016. Paleo-marine environments of the early Cambrian Yangtze Platform. Palaeogeogr. Palaeoclimatol. Palaeoecol. 443, 66–79.
Zhang, H., Fan, H., Wen, H., Zhu, X., Tian, S., 2020. Oceanic chemistry recorded by cherts during the early Cambrian Explosion, South China. Palaeogeogr. Palaeoclimatol. Palaeoecol. 558, 109961.
Zhao, G., Wang, Y., Huang, B., Dong, Y., Li, S., Zhang, G., Yu, S., 2018. Geological reconstructions of the East Asian blocks: from the breakup of Rodinia to the assembly of Pangea. Earth Sci. Rev. 186, 262–286.
Zhou, M.F., Ma, Y., Yan, D.P., Xia, X., Zhao, J., Sun, M., 2006. The Yanbian terrane (Southern Sichuan Province, SW China): a Neoproterozoic arc assemblage in the western margin of the Yangtze block. Precambrian Res. 144, 19–38.
Zhou, L., Wang, Z., Gao, W., Zhang, K., Li, H., Zhang, L., 2019. Provenance and tectonic setting of the lower Cambrian Niutitang formation shales in the Yangtze platform, South China: implications for depositional setting of shales. Geochemistry 79 (2), 384–398.
Zhu, M.Y., Babcock, L.E., Peng, S.C., 2006. Advances in Cambrian stratigraphy and paleontology: integrating correlation techniques, paleobiology, taphonomy and paleoenvironmental reconstruction. Palaeoworld 15, 217–222.
Zhu, M., Yang, A., Yuan, J., Li, G., Zhang, J., Zhao, F., Ahn, S.Y., Miao, L., 2019. Cambrian integrative stratigraphy and timescale of China. Sci. China Earth Sci. 62, 25–60.